



AD-A279 213

NRL/MR/6721--94-7453



X-Ray Laser Program Final Report for FY93

COMPILED BY
JOHN P. APRUZESE

*Radiation Hydrodynamics Branch
Plasma Physics Division*



April 25, 1994

94-14548



SAP

DTIC QUALITY CONTROL

Approved for public release; distribution unlimited.

94 5 13 104

REPORT DOCUMENTATION PAGE

Form Approved
OMB No. 0704-0188

Public reporting burden for this collection of information is estimated to average 1 hour per response, including the time for reviewing instructions, searching existing data sources, gathering and maintaining the data needed, and completing and reviewing the collection of information. Send comments regarding this burden estimate or any other aspect of this collection of information, including suggestions for reducing this burden, to Washington Headquarters Services, Directorate for Information Operations and Reports, 1215 Jefferson Davis Highway, Suite 1204, Arlington, VA 22202-4302, and to the Office of Management and Budget, Paperwork Reduction Project (0704-0188), Washington, DC 20503.

1. AGENCY USE ONLY (Leave Blank)	2. REPORT DATE April 25, 1994	3. REPORT TYPE AND DATES COVERED	
4. TITLE AND SUBTITLE X-Ray Laser Program Final Report for FY93		5. FUNDING NUMBERS PE - 63220C	
6. AUTHOR(S) Compiled by John P. Apruzese, authors identified in subsections		8. PERFORMING ORGANIZATION REPORT NUMBER NRL/MR/6721-94-7453	
7. PERFORMING ORGANIZATION NAME(S) AND ADDRESS(ES) Naval Research Laboratory Washington, DC 20375-5320		9. SPONSORING/MONITORING AGENCY NAME(S) AND ADDRESS(ES) Ballistic Missile Defense Organization T/IS Pentagon Washington, DC 20301-7100	
11. SUPPLEMENTARY NOTES This work was supported by the Ballistic Missile Defense Organization under Job Title, Ultra Short Wavelength Laser Research.			
12a. DISTRIBUTION/AVAILABILITY STATEMENT Approved for public release; distribution unlimited.		12b. DISTRIBUTION CODE	
13. ABSTRACT (Maximum 200 words) This report details the progress achieved by the Radiation Hydrodynamics Branch in X-Ray Laser experiments and modeling during FY93. Some of the experimental work discussed was carried out at Sandia National Laboratories in collaboration with NRL. It is divided into an executive summary and sections whose authors are separately identified. The individual sections describe progress in photopumped x-ray laser research, inversions and gain in plasmas which can be created by ultraintense subpicosecond lasers, and prospects for achieving a Ly α laser.			
14. SUBJECT TERMS X-ray laser Neonlike lasers Resonant photoexcitation		Population inversion Ultra short pulse lasers Pulsed power	Transient transport phenomena Spectroscopy X-ray pulsewidth
17. SECURITY CLASSIFICATION OF REPORT UNCLASSIFIED		15. NUMBER OF PAGES 60	
18. SECURITY CLASSIFICATION OF THIS PAGE UNCLASSIFIED		16. PRICE CODE	
19. SECURITY CLASSIFICATION OF ABSTRACT UNCLASSIFIED		20. LIMITATION OF ABSTRACT UL	

TABLE OF CONTENTS

EXECUTIVE PROGRAM SUMMARY.....iv

A. Residual energy and its effect on gain gan in a Ly α laser.....1

B. Ultrashort laser produced Al/Si plasma.....25

C. Short pulse driven selenium x-ray lasers.....41

Accession For	
NTIS GRA&I	<input checked="" type="checkbox"/>
DTIC TAB	<input type="checkbox"/>
Unannounced	<input type="checkbox"/>
Justification	
By _____	
Distribution/Avail _____	
Availability Codes	
Dist	Avail and/or Special
A-1	

EXECUTIVE PROGRAM SUMMARY

In this NRL Memorandum Report we describe the x-ray laser research conducted by the Radiation Hydrodynamics Branch under BMDO sponsorship during FY 1993. Some of the experimental work was performed at Sandia National Laboratories in collaboration with NRL. This document consists of three sections whose authors are separately identified, each covering in detail the progress in a different aspect of the overall effort.

The work of FY 1993 has brought exciting insights and discoveries relevant to both principal categories of x-ray laser drivers. In general, the energizers of x-ray lasers may be divided into two broad groups, energy-rich and intensity-rich. The most energy-rich drivers are the large pulsed-power generators, which can dump tens of kilojoules or more into a plasma in tens of nanoseconds, via an electrical discharge. The most intensity-rich drivers are the new ultrashort pulse lasers which, while usually coupling a joule or less to the medium, do it in a fraction of a picosecond, over a small focused area yielding intensities of 10^{18} W cm⁻² or higher. Both types of systems have specific advantages. A discharge driver is able to produce a relatively long radiation pulse containing considerable energy. A short-pulse laser, on the other hand, has the singular capability to decouple the ionization state of the plasma from its temperature. This effect can occur because field ionization dominates the usual collisional processes, or, alternatively, because the heating of the electrons outpaces ionization in those cases where collisional effects are important. In either instance, a uniquely nonequilibrium plasma results which can be highly conducive to inversions and gain.

For several years, the Na-Ne resonantly photopumped x-ray laser has been pursued in collaboration with Sandia National Laboratories on the Saturn facility at Sandia, the world's most powerful Z-pinch driver. This effort has already resulted in the first and to date the only demonstration of an x-ray population inversion driven by photopumping. During FY 1993 a noteworthy event in this continuing research was the first, and quite strong, detection of the photopumped 4-2 He-like line complex at 58 Å. No attempt has been made to measure gain and indeed, this wavelength is not one at which gain is

expected for this experiment. However, x-ray laser work has been replete with instances of both unexpected gain and unexpected lack of gain, and in many cases the underlying physical causes are still unresolved. Relative to the 3-2 complex at 78 \AA , the observed strength of this line is at least a factor of two greater than that predicted by either the NRL or Lawrence Livermore National Laboratory models. The lines which are expected to show the greatest gain under the Sandia experimental conditions, namely, the 4-3 singlets near 230 \AA , have not yet been seen. For a number of reasons whose details are inappropriate for a summary, it is believed that these lines are obscured by anomalously high opacity of the plastic window which retains the neon in the gas cell. Relatively minor modifications of this experiment ought to be able to more effectively use the radiation of the Na pinch to fully ionize this window and thereby reduce its absorption.

One of the most attractive methods to reduce the wavelength and increase the efficiency of an x-ray laser is to drive an inversion relative to the ground state of an atom or ion. For instance, for the Ly α line of a hydrogenic species, the transition energy is 75% of the ionization potential, compared to 14% for the 3-2 line which can lase via recombination. The 2-1 Ly α line can also be inverted by recombination pumping, but it is a very difficult task due to the rapid fillup and slow emptying of the ground state. This is where the new ultrashort lasers can serve a critical and at present irreplaceable role. By stripping an ion completely and rapidly, these devices allow the development of transient inversions which could lead to gain in Ly α . The first section of this report presents a comprehensive analysis of the both the laser specifications and plasma conditions necessary to achieve gain in the Ly α lines of both H and He. It is found that for these elements, existing systems are capable of demonstrating such a laser.

A fundamental analysis of the interaction of such short-pulse lasers with a target is presented in the second section. The comprehensive model described therein includes detailed atomic physics of both Al and Si, non-LTE radiation hydrodynamics, and a Helmholtz wave solution for the laser field. The role of energetic electrons in creating K shell vacancies is explored. The use of thin multiple layers is a potentially promising method of obtaining information about ionization and (possibly) also the electron energy distribution. In some of the upper states of Li-like Al, inversions are calculated to develop

in the blowoff plasma for the higher laser intensities considered.

The final section demonstrates dramatically the effect that decoupling the temperature and ionization state in the presence of transient population behavior can have on the gain of a well-known, proven laser system. In the case of Ne-like Se, gains exceeding 600 cm^{-1} are calculated for pump laser intensities above $3 \times 10^{16} \text{ W cm}^{-2}$. This is more than two orders of magnitude greater than present experimentally observed values. However, given the availability of superintense, ultrashort-pulse lasers, there are sound physical reasons underlying the feasibility of such a huge amplification. Among the important processes in the plasma is the lagging of the ionization state behind the electron temperature. In the case under study, Ne-like Se ions are exposed to collisional excitation by electrons much hotter than would occur in a plasma closer to collisional-radiative equilibrium. This results in considerably faster excitation of the upper laser levels, and is responsible in part for the much greater predicted gain.

Residual energy and its effect on gain in a Lyman α laser

P. Pulsifer, J.P. Apruzese, J. Davis and P. Kepple

Radiation Hydrodynamics Branch

Plasma Physics Division

Abstract

To examine prospects for gain in a Lyman α recombination laser driven by a high-intensity, short-pulse laser, we calculate the residual energy in both hydrogen and helium during recombination after the ionizing pulse. The expected gain as a function of residual energy and density is then separately evaluated. The residual energy calculation includes above-threshold ionization (ATI) in the presence of a background plasma, as well as inverse bremsstrahlung heating. At electron densities over 10^{18} cm^{-3} but below critical density, the plasma reduces the ATI energy by approximately a factor of two, but without a previously-reported dependence on the pulsewidth. Inverse-bremsstrahlung heating can be significant, but is not dominant for the parameters considered. Detailed recombination-laser gain calculations were performed for the Ly α transitions of both H and He, using Stark profiles to represent the laser line cross section. To obtain gain of near 2 cm^{-1} lasting at least a few ps, the H plasma temperature must be less than 3.5 eV and electron density between 4×10^{17} to $4 \times 10^{18} \text{ cm}^{-3}$; for He, the temperature must be less than 15 eV and electron density between 2×10^{18} and $2 \times 10^{19} \text{ cm}^{-3}$. Our calculations indicate that these conditions can be satisfied for H, if the driving laser intensity is above $4 \times 10^{14} \text{ W cm}^{-2}$, and for He, if the laser intensity is above $1.7 \times 10^{16} \text{ W cm}^{-2}$ and wavelength is below $0.6 \mu\text{m}$.

I. Introduction

The possibility of developing a recombination x-ray laser which is driven by the new short-pulse, high-intensity table-top lasers has recently been considered.^{1,2,3,4,5} With sufficiently high intensity, a population inversion can be obtained with large transition energies (such as those involving the ground state), which can generate significant gain at UV or soft x-ray wavelengths. These schemes require both that the atoms initially be ionized above the lasing stage and that the residual energy of the electrons be low to facilitate recombination and suppress collisional excitation.

In this paper, we analyze the conditions required for gain on the Lyman α transitions of both hydrogen (1216 Å) and helium (304 Å). Such lasers were initially proposed some years ago.⁶ Our gain calculations are based on fully self-consistent Stark profiles for the completely stripped background gas. The residual energy is calculated including the electron above-threshold-ionization (ATI) energy, a simple model of plasma effects, and inverse-bremsstrahlung, or collisional, heating.

To obtain the ATI energy, we follow a well established procedure^{1,7} and solve for the classical (non-relativistic, non-quantum) electron motion; the ATI energy is just the electron's energy long after the pulse has passed (after several ps, when recombination is occurring).

PIC simulations⁸ have indicated that space-charge, or plasma effects, might in some way significantly enhance or diminish the energy absorption of the target medium. For short pulse lengths, comparable to the inverse plasma frequency, space-charge heating apparently stems from the non-adiabatic ponderomotive expulsion of electrons (electron cavitation), which induces plasma oscillations. An earlier study⁸ sought to model plasma effects on ATI energy by including the plasma frequency in the single-electron equation of motion; it found that the plasma-modified ATI energy was fairly large, but oscillated by several orders of magnitude as a function of electron density and pulse period. Here, we use the same model, but our findings disagree with those results: the ATI energy is much lower, and there are no oscillations with electron density. For this simple model, the principal effect of a background plasma is to substantially increase the residual energy near the critical surface. These results are more in accord with those of other recent theoretical and experimental papers,^{9,10} are not inconsistent with the PIC simulations in Ref. 8, and are in fact more favorable to the success of a Ly α laser.

One potentially important factor that has not been widely considered is inverse bremsstrahlung heating.⁹ Simple scaling arguments indicate that this could be a much larger source of energy to the plasma than the ATI mechanism. In fact, for the parameters we consider, inverse bremsstrahlung does not turn out to be the most important source of heating, largely because the high quiver energy of the electrons in the field makes the electron-ion collisional cross section small during the bulk

of the heating.

The organization of this paper is as follows. In Section II, we consider ionization and electron heating by the laser pulse, and show how to obtain the residual energy during recombination. In Section III, we consider the recombination process, and show what conditions must be satisfied by the plasma to obtain significant gain. These results will show the optimal pump laser parameters for driving the recombination laser. Possible experimental parameters are discussed in the final section.

II. Calculation of electron residual energy

We consider a laser pulse of wavelength λ (in μm) and peak intensity I (in W cm^{-2}), incident onto an initially neutral gas, which has atomic charge Ze . (An electron has charge $-e$ and mass m). The laser pulse profile is assumed to be such that the electric field is given by $E(t) = E_{env}(t) \sin \omega t$, with the pulse envelope given by

$$E_{env}(t) = E_0 \operatorname{sech} \left[\frac{2(t - t_{max})}{\tau_p} \right] \quad (1)$$

and the peak electric field $E_0 = \sqrt{240\pi I}$ (in V/cm). For the calculations presented here, we consider a pulse width $\tau_p = 100$ fs and time of maximum intensity $t_{max} = 200$ fs. The intense laser field multiply ionizes the gas, and the ion densities n_i (in cm^{-3}) for charge state $Z_i = i$ evolve according to the coupled system of equations

$$\frac{dn_i}{dt} = W_i n_{i-1} - W_{i+1} n_i, \quad (2)$$

where W_i is the rate of ionization from charge state Z_{i-1} to Z_i , and $n_{-1} = W_{Z+1} \equiv 0$. The evolving electron density is $n_e = \sum_i Z_i n_i$. We assume that the laser pulse duration is much shorter than the recombination time, so that during the pulse recombination can be neglected.

There are various theories of ionization in the strong-field regime.⁷ For ATI conditions, considered here, the photon energy ($\hbar\omega = 1.24/\lambda$ eV) is less than the ionization energy U_i , which in turn is less than or equal to the electron quiver energy (defined below). Here, tunneling ionization might be expected to dominate, and the ionization rate can be obtained from either Keldysh¹¹ or Ammosov et al.¹² For the calculations presented here, we use the Ammosov formula,¹² which has some experimental support,¹³ and is also considerably simpler to evaluate. The Ammosov rate is

$$W_i(E) = 1.61 \omega_{a.u.} \frac{Z_i^2}{n_i^{*4.5}} \left[10.87 \frac{Z_i^3}{n_i^{*4}} \frac{E_{a.u.}}{E} \right]^{2n_i^* - 1.5} \exp \left[-\frac{2Z_i^3}{3n_i^{*3}} \frac{E_{a.u.}}{E} \right] \quad (3)$$

where $\omega_{a.u.} = 4.1340 \times 10^{16} \text{ sec}^{-1}$, n_i^* is the effective principal quantum number for a hydrogenic atom:

$$n_i^* = \frac{Z_i}{\sqrt{U_i/13.6 \text{ eV}}}, \quad (4)$$

and $E_{a.u.} = 5.1421 \times 10^9$ V/cm is the electric field at a ground-state hydrogen electron.

At the time of ionization, we assume that electrons have zero energy;¹ thereafter, they are (classically) accelerated by fields from the laser and from the surrounding plasma.⁸ Most of the electron energy during the laser pulse comes from the oscillatory quiver motion in the laser field, and is returned to the field when the pulse passes. The relatively small residual energy after the pulse leaves is the ATI energy. When the effect of the plasma is ignored, the ATI energy is the time-independent part of the energy, which is determined by the wave phase at ionization. With a plasma oscillation present, there is no time-independent part of the energy, so the ATI energy must be an average energy. To find it, we follow the classical trajectory $\mathbf{x}(t)$ of an electron, with the effect of the charge cloud of the surrounding plasma being treated solely as a spring-like restraining force⁸ parameterized by the plasma frequency $\omega_p = \sqrt{4\pi n_e e^2/m}$:

$$\ddot{\mathbf{x}} + \omega_p^2 \mathbf{x} = -\frac{e}{m} \mathbf{E}(t). \quad (5)$$

The required boundary condition on Eq. (5) is that $\dot{\mathbf{x}} = 0$ at the ionization time $t = t_0$. With the additional imposed condition that $\mathbf{x}(t_0) = 0$, the general solution to Eq. (5) can be expressed as

$$\mathbf{x}(t) = -\frac{\cos \omega_p t}{\omega_p} \int_{t_0}^t \frac{e\mathbf{E}(t)}{m} \sin \omega_p t dt + \frac{\sin \omega_p t}{\omega_p} \int_{t_0}^t \frac{e\mathbf{E}(t)}{m} \cos \omega_p t dt. \quad (6)$$

If the electric field envelope were constant, as it roughly is near the peak of the pulse, the solution would be similar to that obtained elsewhere:⁸

$$\mathbf{x}(t) = \frac{eE_{env}}{m(\omega^2 - \omega_p^2)} \left\{ -\sin \omega t + [\omega \cos \omega t_0 \cos \omega_p t_0 + \omega_p \sin \omega t_0 \sin \omega_p t_0] \sin \omega_p t \right. \\ \left. + [-\omega \cos \omega t_0 \sin \omega_p t_0 + \omega_p \sin \omega t_0 \cos \omega_p t_0] \cos \omega_p t \right\}. \quad (7)$$

This describes the complicated electron motion during the pulse, but is not really useful for finding the ATI energy, which is determined much later. The electron motion at those late times, obtained from the $t \rightarrow \infty$ limit of eq. (6), is just simple oscillation at the plasma frequency:

$$\dot{\mathbf{x}}(t_0, t) = \frac{eE_0}{m} [A \sin \omega_p t + B \cos \omega_p t] \quad (8)$$

with

$$A(t_0) \equiv \int_{t_0}^{\infty} \text{sech} \left[\frac{2(t - t_{max})}{\tau_p} \right] \sin \omega t \sin \omega_p t dt \quad (9)$$

$$B(t_0) \equiv \int_{t_0}^{\infty} \text{sech} \left[\frac{2(t - t_{max})}{\tau_p} \right] \sin \omega t \cos \omega_p t dt \quad (10)$$

The time-dependence of the factors A and B can be ignored because the laser pulse (sech) vanishes for late time; they depend only on the time t_0 when the electrons are ionized. If the plasma period

is smaller than the times of interest (the ns recombination time), the single-electron ATI energy is the electron energy averaged over the plasma-frequency motion:

$$\epsilon(t_0) \equiv \frac{1}{2} m \langle \dot{x}^2 \rangle = \epsilon_q \omega^2 (A^2 + B^2) \quad (11)$$

where

$$\epsilon_q \equiv \frac{e^2 E_0^2}{4m\omega^2} \quad (12)$$

is the quiver, or ponderomotive, energy.

The average electron residual energy $\langle \epsilon \rangle$ after the passage of the pulse is given by the sum of the number of electrons generated at each t_0 times the residual energy of these electrons:

$$\langle \epsilon \rangle = \frac{\sum_{j=1}^{x_{\max}} \int_0^{2t_{\max}} n_j(t_0) W_j(E(t_0)) \epsilon(t_0) dt_0}{\sum_{j=1}^{x_{\max}} \int_0^{2t_{\max}} n_j(t_0) W_j(E(t_0)) dt_0} \quad (13)$$

The upper limit of integration is chosen as $2t_{\max}$ here simply for convenience, to make the integration domain symmetrical over the pulse; the results should not be sensitive to the value chosen for this limit, as long as the pulse amplitude is small there. For simplicity, the influence of the space-charge field on the ionization rate $W(E)$ has been neglected, although PIC simulations⁸ have indicated that electron cavitation, when significant, can produce a space-charge electric field comparable to the laser field $E(t)$. The simple model used here could be extended in that case by deducing the space-charge field at the points of interest (subject to details of pulse profile and ionization dynamics) and then using the total field in eq. (13). We define the residual electron temperature to be proportional to the average energy:

$$T = \frac{2}{3} \langle \epsilon \rangle. \quad (14)$$

When the laser pulse width is very broad compared to the oscillator frequency and plasma frequency (i.e., $\omega \tau_p \gg 1$ and $\omega_p \tau_p \gg 1$), then the integrals of A and B can be approximately evaluated, and

$$\epsilon(t_0) \approx \frac{e^2 E(t_0)^2}{4m} \left[\frac{\omega_p^2 \sin^2 \omega t_0 + \omega^2 \cos^2 \omega t_0}{(\omega^2 - \omega_p^2)^2} \right]. \quad (15)$$

This expression shows that, long after the pulse, plasma effects do not decrease the residual energy. There is no periodic dependence on the plasma frequency in the residual energy, as was asserted elsewhere.⁸ That periodic variation was based on an ATI energy calculated from some average of Eq. (7), and so incorrectly included electron motion during the pulse in the ATI energy calculation. In fact, plasma effects can increase the residual energy, but the effect is not important except near

the critical surface, where the plasma and wave frequencies are near resonance and the residual energy becomes very large.

When the density is zero (no plasma) the single-particle ATI energy from Eq. (15) is

$$\epsilon(t_0) = \epsilon_q \cos^2 \omega t_0 \quad (16)$$

which is half the standard zero-density result.¹ The factor of two difference is due to the averaging over a plasma period performed in Eq. (15); this averaging makes sense only when the plasma frequency is large, while for low densities the peak value of the electron energy should be used. The density effect on residual energy depends on the ratio $\omega_p^2/\omega^2 = n_e/n_{crit}$, where $n_{crit} = 1/2 \times 10^{21}/\lambda^2$ is the critical density, where the plasma becomes opaque to the laser radiation. The single-particle ATI energy from Eq. (15) is shown in Fig. (1), where separate curves are drawn for different ionization phases ωt_0 . As the density approaches n_{crit} , the ATI energy sharply increases, and becomes less dependent on the time of ionization t_0 .

Evidently, plasma does not significantly increase the ATI energy at much less than $0.1 n_{crit}$. For 1.06 μm Nd:glass laser light, the $n_{crit} = 10^{21} \text{ cm}^{-3}$, while for a 248 nm KrF laser $n_{crit} = 2 \times 10^{22} \text{ cm}^{-3}$; thus, according to our simple model, plasma modification of the ATI energy is not a significant factor below densities of 10^{20} cm^{-3} .

Collisional heating from inverse bremsstrahlung is potentially important, possibly dominant, in dense laser-heated plasmas.⁹ The inverse bremsstrahlung heating rate is given by

$$\dot{E}_{IB} = \frac{4\pi}{3} \epsilon_q \nu_{ei} v_{th}^3 f_0(0) F(v_0/v_{th}) \quad (17)$$

where $f_0(v)$ is the isotropic part of the electron distribution function, $v_{th} = \sqrt{2kT/m}$ is the thermal velocity (with kT the electron temperature in energy units),

$$\nu_{ei} = 3.86 \times 10^{-6} \frac{Z n_e}{(kT)^{3/2}} \log \Lambda \quad (18)$$

is the electron-ion collision frequency, with Coulomb logarithm given by

$$\log \Lambda = 22.4 + \log [(kT)^{3/2}/n^{1/2}], \quad (19)$$

and F is a correction factor to the cross section due to the quiver motion of the electrons,¹⁴ which may be approximated

$$F(x) = \frac{1}{1 + 2x^2/3}. \quad (20)$$

The rate \dot{E}_{IB} depends on the electron distribution only through the overall normalization, and is not sensitive to the details of its shape. Therefore, although the laser-produced electrons equilibrate

on the ps to tens of ps timescale (much longer than the pulse width), it is not too inaccurate to approximate the distribution function to be a Maxwellian, so that

$$f_0(0) = n_e \left(\frac{m}{2\pi kT} \right)^{3/2} \quad (21)$$

To estimate the magnitude of inverse-bremsstrahlung heating, we determine the total energy input by time-integrating the heating rate, Eq. (17). The heating rate depends on the time-varying electron density, obtained by solving the rate equations, Eq. (2). The temperature at each time is given by the average energy per particle, as accumulated from ATI (a small term), prior inverse bremsstrahlung heating, and the quiver motion (a large term). The inverse-bremsstrahlung contribution to the final temperature is just the total average energy input per particle:

$$T_{IB} = \frac{2}{3n_e} \int_0^\infty \langle \dot{E}_{IB} \rangle dt \quad (22)$$

The actual residual temperature is given by the sum of contributions from ATI (Eq. (14)) and IB heating (Eq. (22)). Results of residual energy calculations are shown in Figs. 2–5. The contours in Fig. (2) depict the average degree of ionization after the laser pulse of an initially neutral H gas, as a function of laser intensity and wavelength; any laser power above the $\bar{Z} = 1$ contour leaves the gas fully stripped. The contours in Fig. (3) show the residual temperature in eV of the ionized H plasma. The inverse-bremsstrahlung heating rate is proportional to n_e ; here, an atomic density of $2 \times 10^{18} \text{ cm}^{-3}$ was used, where there is relatively high gain. Similarly, Fig. (4) depicts the average degree of ionization after the laser pulse of an initially neutral He gas, and Fig. (5) shows the residual temperature in eV as a function of laser wavelength and intensity. For He, the inverse-bremsstrahlung heating rate was computed using an atomic density of $4 \times 10^{18} \text{ cm}^{-3}$.

III. Conditions required for gain on Ly α for hydrogen and helium

It is reasonable to assume that gain on Ly α via transient recombination⁶ would be easiest to achieve in the lowest atomic number elements. Therefore, we examine H and He closely using time-dependent multilevel gain calculations to establish the electron temperature (i.e., residual energies) and densities at which reasonable amplification would occur. These can be related to the short-pulse laser parameters which are predicted to provide such conditions according to the calculations of Section II. In this way, we specify what would constitute a promising demonstration experiment.

The first and well-known condition for transient gain to the ground state is that the plasma be initially fully stripped.⁶ Therefore, laser irradiances must be used which are at or above those in the contour plots (Figs. 2–5) corresponding to $Z = 1$ for H and $Z = 2$ for He. In all the calculations discussed below, the plasma is assumed initially fully stripped. The atomic level populations are

calculated as a function of time for a fixed assumed density and electron temperature. The ions are assumed to remain cold, since their equilibration time (a few hundred ps) at the densities of interest far exceeds the timescales within which gain is expected. The algorithm of Ref. 15 is employed to integrate the set of rate equations, viz.,

$$\frac{dN_i}{dt} = \sum_{j \neq i} N_j R_{ji} - N_i \sum_{j \neq i} R_{ij} \quad (23)$$

where N_i is the population density of the state i and R_{ji} are the rates connecting all states; these atomic-level rates and densities are not to be confused with the ionization-state rates and densities of Eq. (2).

In Eq. (23), the rates connecting the various levels of the H and He states include collisional excitation and de-excitation, radiative, three-body, and dielectronic recombination, collisional ionization, and radiative decay. Most of the atomic data for these simple and well-studied species are readily available from numerous sources in the literature. Other rates were calculated using standard techniques (e.g., the semiclassical approximation for collisional rates corresponding to radiatively allowed collisions). The levels of the one-electron species are distinguished only by principal quantum number n , although fine structure effects on Ly α are included in the overall Stark profile used in calculating gain.

The highest principal quantum number included in the atomic model is $n = 5$ for both H and He. This is approximately in accord with the Inglis-Teller criterion as updated by Griem (Ref. 16, p. 125): At an electron density of 10^{18} cm^{-3} , Ref. 16 predicts that the series limit occurs at $n = 4-5$ for H, and $n = 6-7$ for He. While we do not include a self-consistent treatment of continuum lowering, it is clearly preferable to truncate the levels at $n = 5$ rather than at some arbitrary higher number (10 or 20, for instance), far above the last discrete level at densities of interest.

The gain g in cm^{-1} on the $n = 2$ to 1 transition of a hydrogenic species is given by

$$g = N_2 \sigma_{21} - N_1 \sigma_{12} \quad (24)$$

where σ_{21} (σ_{12}) are the emission (absorption) cross sections in cm^2 for the transition at the peak of the profile, and the N 's are the population densities of the $n = 1$ and $n = 2$ levels. In Eq. (24) a positive number corresponds to amplification and a negative one to absorption. For Ly α , $\sigma_{21} = \sigma_{12}/4$, and $n = 2$ must have at least 4 times the population of the ground state to obtain gain. Clearly, this can only occur on a transient basis since population tends to pile up in $n = 1$, which has no radiative decay channel. However, three-body recombination from the bare nucleus, per unit statistical weight, is approximately proportional to n^4/T . Therefore, one anticipates a brief period of gain for an appropriate range of sufficiently low temperatures, if $n = 1$ is initially empty.

A key feature of the present work is that we have employed the best available representation of the Ly α cross section, namely self-consistently calculated Stark profiles for both H and He.¹⁷

For H, we find that σ_{12} is approximately given by

$$\sigma_{12}^H = 6.1 \times 10^{-15} \left(\frac{10^{18}}{n_e} \right)^{0.89} T^{0.25} \quad (25a)$$

whereas, for He:

$$\sigma_{12}^{He} = 2.5 \times 10^{-14} \left(\frac{10^{18}}{n_e} \right)^{0.93} \left(\frac{T}{5} \right)^{0.25} \quad (25b)$$

For $T \propto Z^2$, the He cross section exceeds that of H by a factor of 4 at $n_e = 10^{18} \text{ cm}^{-3}$. Partly offsetting this, however, is the fact that there are twice as many H ions per electron as He ions. Therefore, we expect gains of comparable magnitude. Also, note from Eq. (25) that as the density increases, the Stark broadening results in a nearly inversely proportional decrease of the peak cross section. However, gain can still increase with density due to the increase in three-body recombination and the greater number of ions available for stimulated emission.

A subset of the calculations which have been carried out for H and He is presented in Figs. 6–10. There is no lower temperature limit below which gain is not possible; indeed, due to the T^{-1} dependence of three-body recombination, gain increases at lower temperatures, assuming of course that the plasma is initially fully stripped. To obtain a gain of $\sim 2 \text{ cm}^{-1}$ last: g at least a few ps, the electron temperature in a He plasma must be $\leq 15 \text{ eV}$, whereas for H the electrons must be no hotter than 3.5 eV . An upper limit on the density is set by the desired gain duration. Note from Figs. 6–10 that, as expected, the gain increases with density, but decreases with increasing temperature. However, the duration of gain decreases sharply with increased density since the absorbing $n = 1$ level fills up correspondingly more rapidly. For gain duration of at least a few ps, the electron density must be no higher than $\sim 2 \times 10^{19} \text{ cm}^{-3}$ for He, or $4 \times 10^{18} \text{ cm}^{-3}$ for H. Since the lifetime of the H Ly α transition (n -averaged) is 2.1 ns , compared to 133 ps for He, one might initially expect considerably greater gain duration for H. However, the corresponding collisional mixing rates are nearly an order of magnitude faster for H at a given density, and the interplay of these effects results in comparable gain durations for both elements (ranging from a few ps to tens of ps).

Refraction of the x-ray laser beam can pose a serious threat to the practical attainment of amplification, due to the density gradients expected in short-pulse laser-driven plasmas. This issue has been analyzed by Amendt et al.,⁵ who assumed a Gaussian beam profile. If b is the beam waist radius, the x-ray lasing length Z_R is approximately given by

$$Z_R = 1.2b \sqrt{\frac{n_{crit}}{n_e}} \quad (26)$$

where n_{crit} is the critical density, defined above. Typical electron densities for good gain in H and He are 2 and $4 \times 10^{18} \text{ cm}^{-3}$, respectively (cf. Figs. 6–10). We take the beam waist radius to be

13 μm , as measured in a recent demonstration of optical guiding of intense laser beam pulses.¹⁸ For these conditions, Eq. (26) gives a propagation length of 0.3 cm for H and 0.9 cm for the considerably shorter wavelength of the He laser. Figs. 8 and 9 indicate that gain length products (gl) greater than or equal to 4 are achievable for He if $T_e \leq 5$ eV. For H, $T_e \leq 1$ eV is necessary to achieve a similar gl. As pointed out in Ref. 5, a larger beam waist radius would significantly relax these requirements. In addition, the presence of a beam guiding channel¹⁸ with a more favorable refractive index profile would very likely lead to considerably longer propagation lengths.

IV. Summary and conclusions

We have presented a procedure to calculate the residual energy of a plasma during the recombination period after passage of a high-intensity, short laser pulse. We then calculated the expected residual energy and degree of ionization for H and He over a range of wavelengths and laser intensities. These results are shown as contour plots in Figs. 2–5. The inclusion of a plasma oscillation does not significantly modify the residual electron energy (other than the factor of two reduction due to the residual plasma oscillation, as discussed at eq. (16)), as long as the plasma density is not close to the critical density.

While our model does not include it, we do not expect the space-charge heating reported in PIC simulations^{8,10} to be important for parameters where significant gain should be found. The short pulse width limits heating due to instability growth and variations in drift velocities.¹⁰ The laser power required is not ultra-high (i.e., $I \ll 10^{18}$ W cm⁻²), and the density is relatively high, so both electron cavitation and its effect on the final plasma temperature⁸ should be minimal; even if this were not true, electron-cavitation heating seems to be much less important when $\omega_p \tau_p / 2\pi > 1$, which is the case for the high-gain densities given here.

Although certainly not conclusive, it is gratifying to note that our results are close to recent experimental measurements by Mohideen et al.¹⁹ Their experiment measured residual energy in a low-density (7×10^8 atoms cm⁻³) He gas, where the factor of 1/2 from averaging over the late-time plasma oscillation in eq. (16) should be omitted. The laser wavelength was 0.820 μm , with intensity 7×10^{15} W cm⁻² and pulsewidth 180 fs. Although their pulsewidth was slightly longer than assumed here (which would tend to increase the residual energy), Fig. (5) shows that for these parameters the predicted residual temperature is roughly 20 eV, compared to the 30 eV measured best-fit temperature.

Through the residual energy and ionization calculations, we have established the plasma conditions during recombination. We have then used an inclusive atomic model to calculate gain and those conditions for which significant gain is obtained. These results are shown in Figs. 6–10. The region in the contour plots where the plasma is both fully stripped and has residual energy

within the given limits is where gain is expected. For H, fully stripped plasma is obtained at intensities above $4 \times 10^{14} \text{ W cm}^{-2}$; the necessary electron temperature, less than 3.5 eV, is satisfied at all wavelengths. For He, fully stripped plasma is obtained when the laser intensity is above $1.7 \times 10^{16} \text{ W cm}^{-2}$; if this is true, the electron temperature is below the maximum 15 eV when the wavelength is below $0.6 \mu\text{m}$.

The minimum density for which adequate gain is obtained can be seen from Figs. 6–10 to be roughly 10^{18} cm^{-3} . Although the residual energy increases with increased density, mostly because of inverse bremsstrahlung, the most important effect is the decrease in gain duration (for a fixed residual energy) with increased density; this limits the electron density to roughly $4 \times 10^{18} \text{ cm}^{-3}$ for H, or $2 \times 10^{19} \text{ cm}^{-3}$ for He.

The simple model used here notably omits consideration of collisions. At typical laser-heated plasma parameters of $kT=10 \text{ eV}$ and $n = 2 \times 10^{18} \text{ cm}^{-3}$, the collision time is about 0.8 ps. Thus, these plasmas are marginally collisional, and collision effects should be studied. Still, collisions do not clearly dominate, and there is probably some validity, at least for simple estimates, to the residual electron energies given here.

References

1. N.H. Burnett and P.B. Corkum, *J. Opt. Soc. Am. B* **6**,1195 (1989).
2. P. Amendt, D.C. Eder and S.C. Wilks, *Phys. Rev. Lett.* **66**,2589 (1991).
3. D.C. Eder, P. Amendt and S.C. Wilks, *Phys. Rev.* **A45**,6761 (1992).
4. P. Amendt, D.C. Eder, R.A. London and M.D. Rosen, *Phys. Rev.* **A47**,1572 (1993).
5. P. Amendt, D.C. Eder, R.A. London, B.M. Penetrante and M.D. Rosen, in *Short-Pulse High-Intensity Lasers and Applications*, edited by H.A. Baldis, SPIE Conf. Proc. No. 1860 (SPIE, Bellingham, WA, 1993), p. 140.
6. W.W. Jones and A.W. Ali, *Appl. Phys. Lett.* **26**,450 (1975); *J. Appl. Phys.* **48**,3118 (1977).
7. R.R. Freeman and P.H. Bucksbaum, *J. Phys. B: At. Mol. Opt. Phys.* **24**,325 (1991).
8. B.M. Penetrante and J.N. Bardsley, *Phys. Rev A* **43**,3100 (1991).
9. S.C. Rae and K. Burnett, *Phys. Rev. A* **46**,2077 (1992).
10. W.P. Leemans, C.E. Clayton, W.B. Mori, K.A. Marsh, P.K. Kaw, A. Dyson, C. Joshi and J.M. Wallace, *Phys. Rev.* **A46**,1091 (1992).
11. L.V. Keldysh, *Sov. Phys. JETP* **20**,1307 (1965).
12. M.V. Ammosov, N.B. Delone and V.P. Kraĭnov, *Sov. Phys. JETP* **6**,1191 (1986).
13. S. Augst, D. Strickland, D.D. Meyerhofer, S.L. Chin and J.H. Eberly, *Phys. Rev. Lett.* **63**,2212 (1989).
14. L. Schlessinger and J. Wright, *Phys. Rev. A* **20**,1934 (1979).
15. T.R. Young and J.P. Boris, *J. Phys. Chem.* **81**,2424 (1977).
16. H.R. Griem, *Plasma Spectroscopy* (McGraw-Hill, N.Y., 1964).
17. P.C. Kepple, *Phys. Rev.* **A6**,1 (1972).
18. C.G. Durfee III and H.M. Milchberg, *Phys. Rev. Lett.* **71**,2409 (1993).
19. U. Mohideen, M.H. Sher, H.W.K. Tom, G.D. Aumiller, O.R. Wood III, R.R. Freeman, J. Bokor and P.H. Bucksbaum, *Phys. Rev. Lett.* **71**,509 (1993).

Figure Captions

Figure 1. Effect of the plasma oscillation on the single-particle ATI energy. The ATI energy, in units of the quiver energy ϵ_q , is shown as a function of density, in units of the critical density n_{crit} , for different times of ionization within the pulse ωt_0 . The solid line is for $\omega t_0 = 0$, when the zero-density ATI energy is maximum; the dashed line is for $\omega t_0 = \pi/4$; and the dotted line is for $\omega t_0 = \pi/2$, when the zero-density ATI energy is zero.

Figure 2. Residual ionization contours for initially neutral H. Contours represent average ionization level $\bar{Z} = n_e/n_H$; for laser intensity above the $\bar{Z} = 1$ contour, the gas is left fully stripped.

Figure 3. Contours of residual temperature in eV of H, as described in Fig. (2). For inverse-bremsstrahlung heating calculations, an initial atomic density of $2 \times 10^{18} \text{ cm}^{-3}$ is assumed.

Figure 4. Residual ionization contours for initially neutral He. Contours represent average ionization level $\bar{Z} = n_e/n_{He}$; for laser intensity above the $\bar{Z} = 2$ contour, the gas is left fully stripped.

Figure 5. Contours of residual temperature in eV of He, as described in Fig. (4). For inverse-bremsstrahlung heating calculations, an initial atomic density of $4 \times 10^{18} \text{ cm}^{-3}$ is assumed.

Figure 6. Ly α gain coefficient for H as a function of time, assuming an initially fully-stripped plasma of the indicated atomic densities. Electron temperature is 1 eV; ions are assumed cold, and Stark profiles are employed to obtain the gain cross section.

Figure 7. As in Fig. 6 except that the electron temperature is 2 eV.

Figure 8. Ly α gain coefficient for He as a function of time, assuming an initially fully-stripped plasma of the indicated atomic densities. Electron temperature is 2 eV; ions are assumed cold, and Stark profiles are employed to obtain the gain cross section.

Figure 9. As in Fig. 8 except that the electron temperature is 5 eV.

Figure 10. As in Figs. 8 and 9, except that the electron temperature is 10 eV.

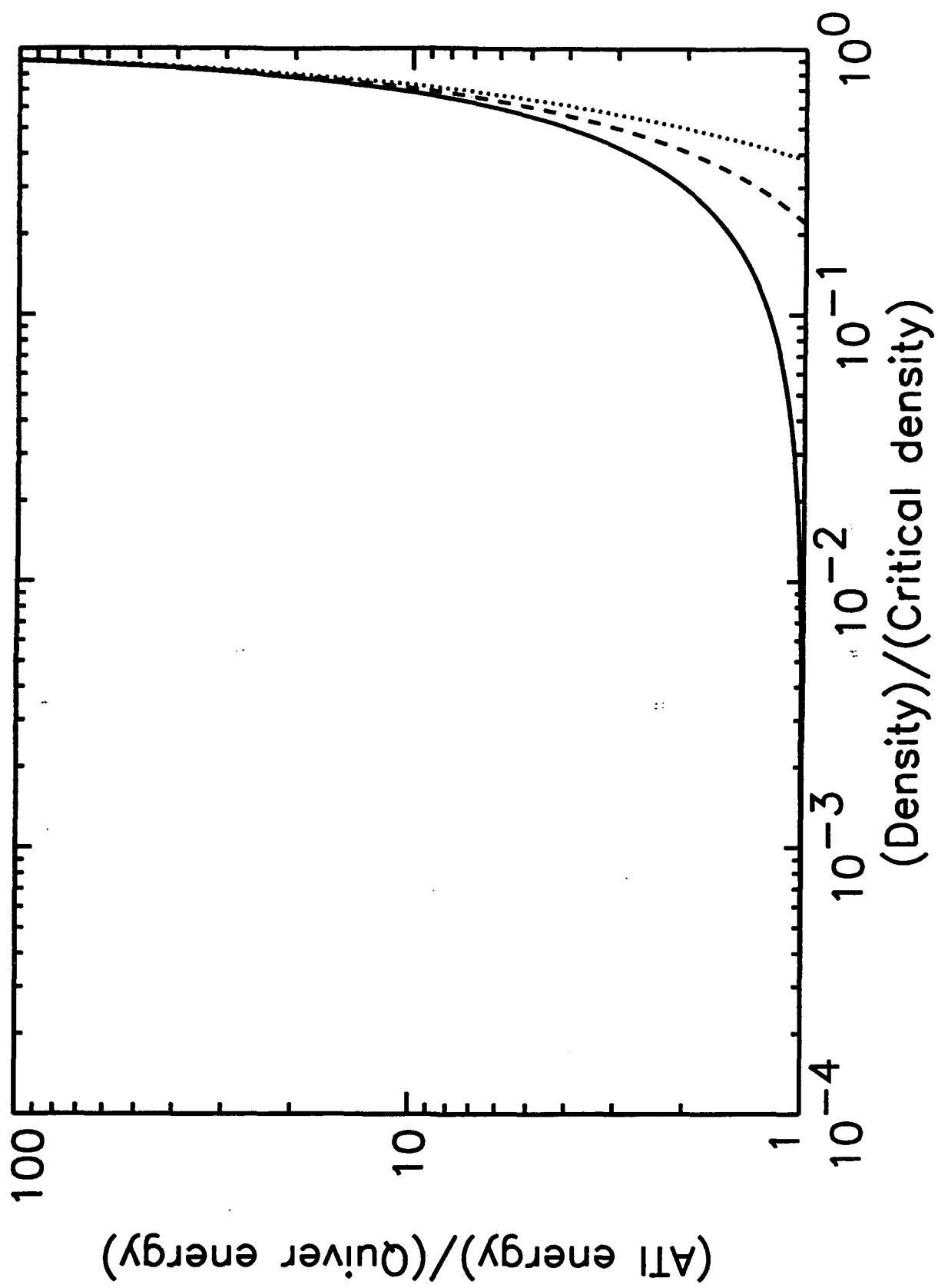


Figure 1

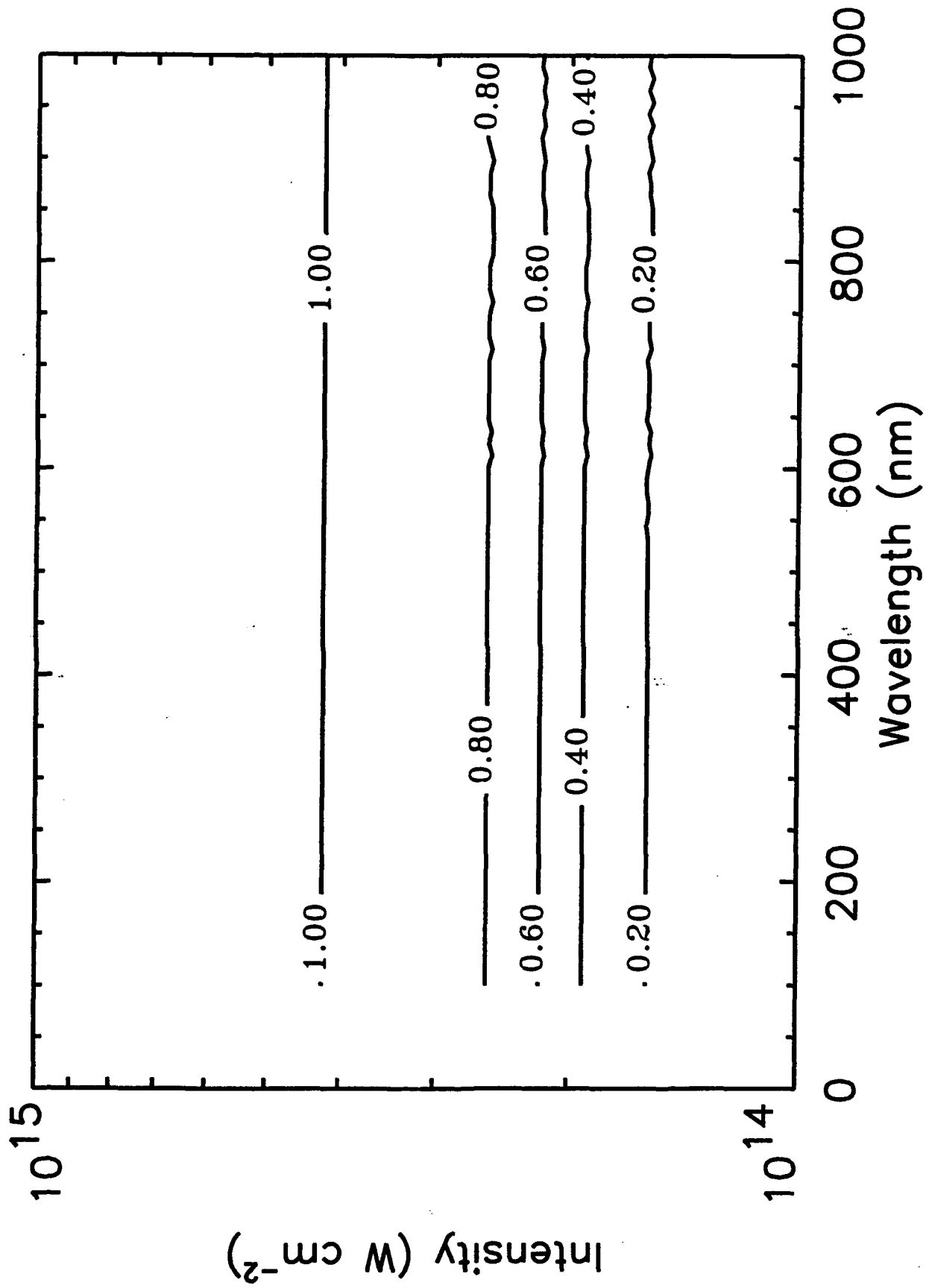


Figure 2

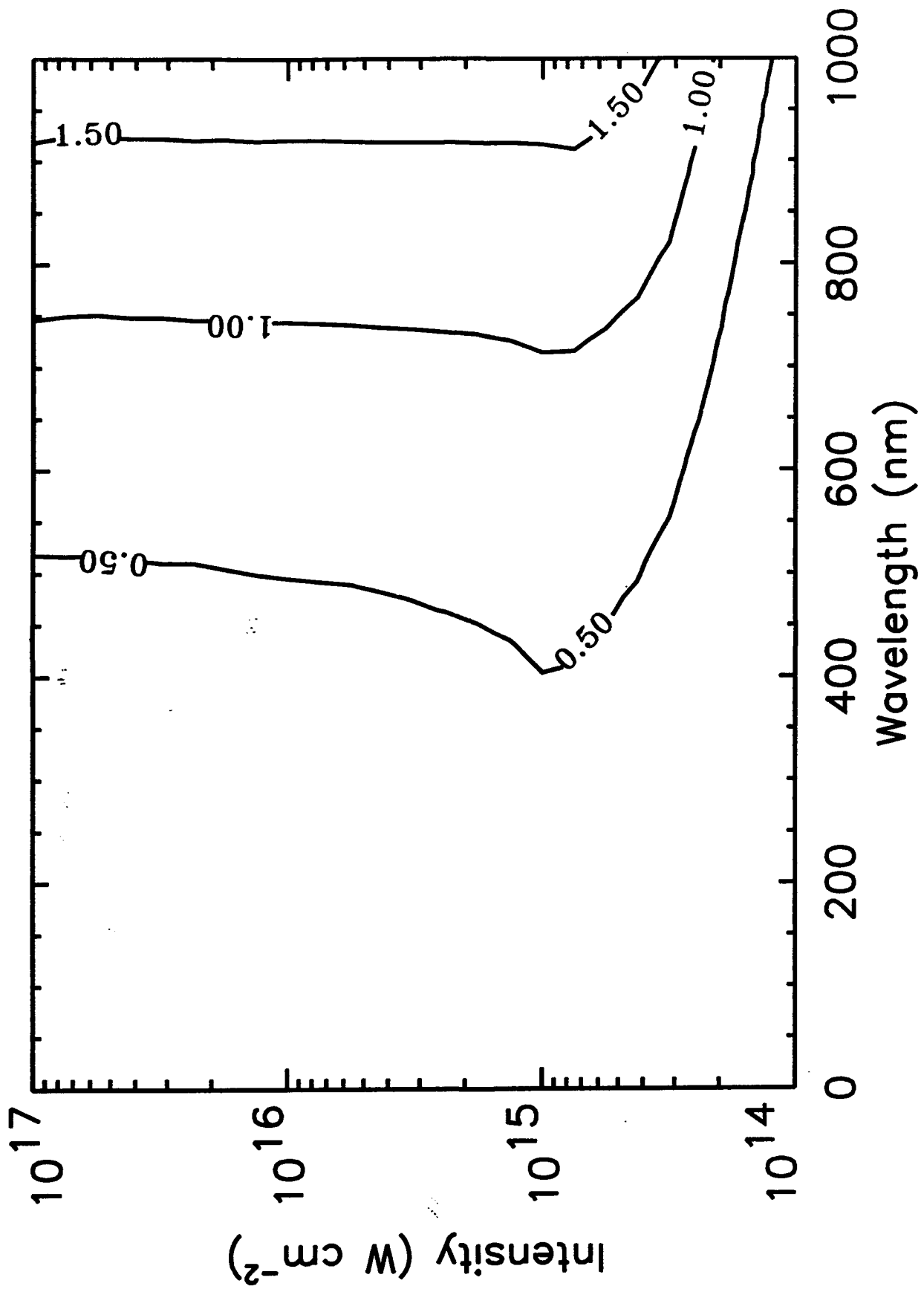


Figure 3

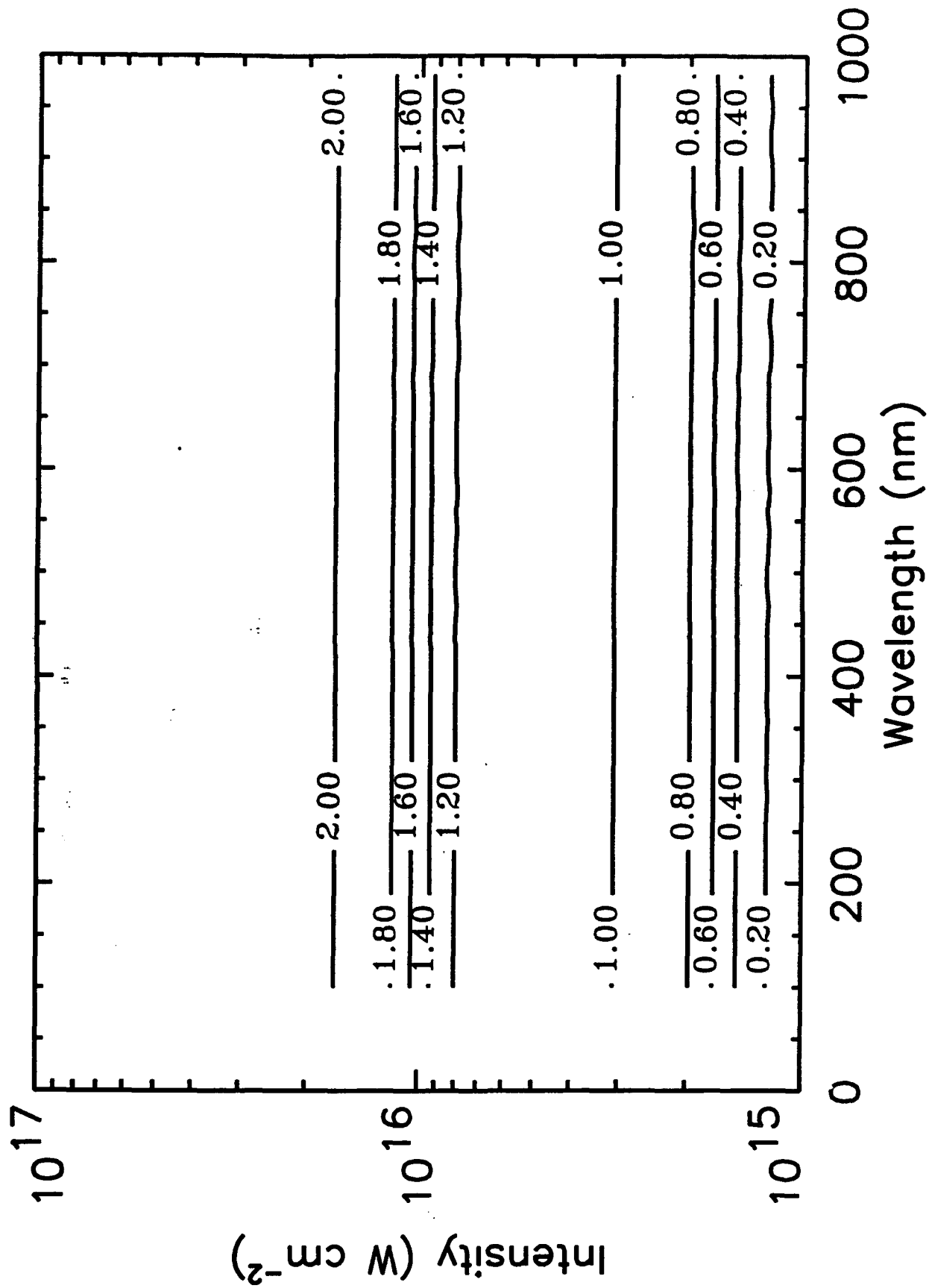


Figure 4

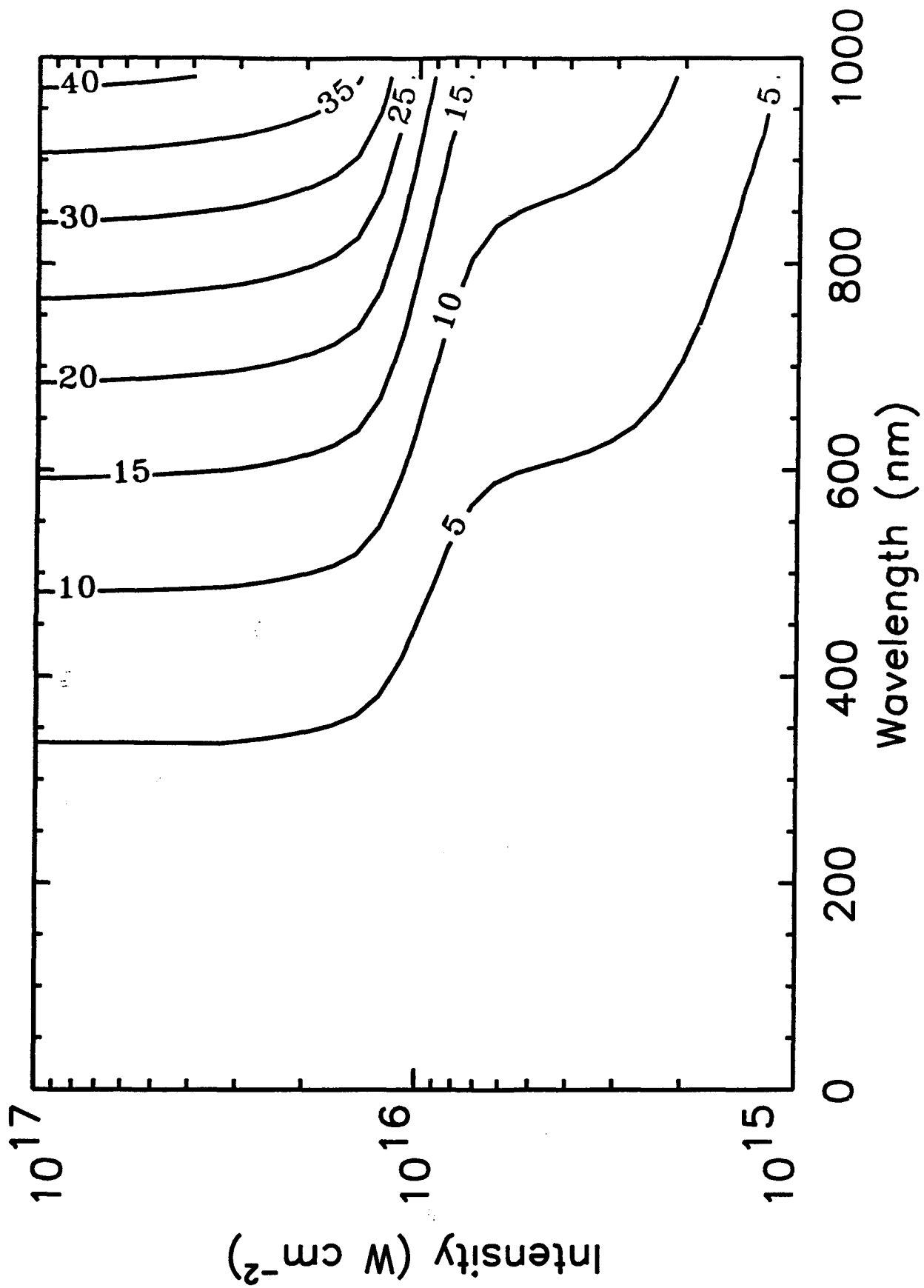


Figure 5

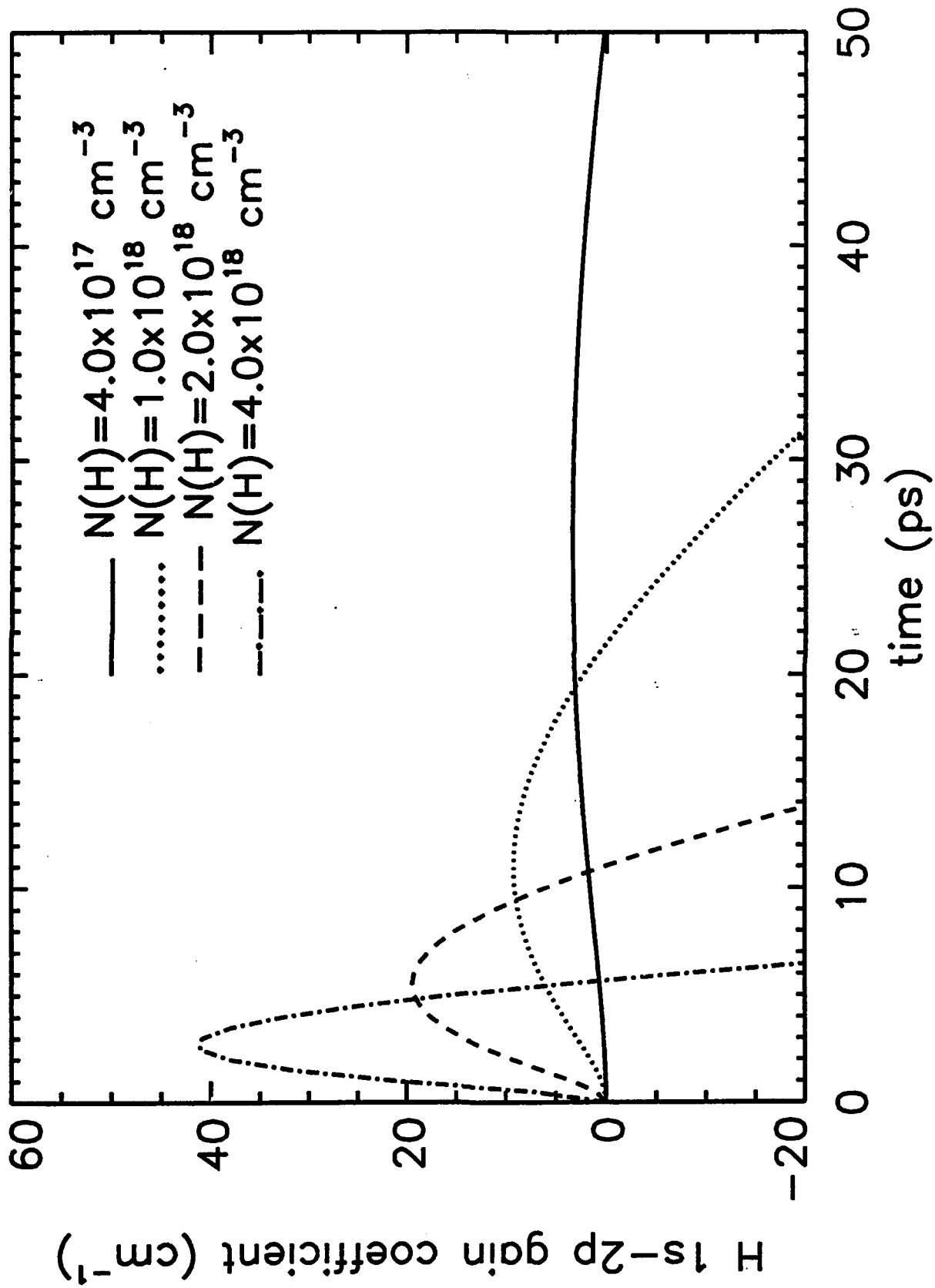


Figure 6

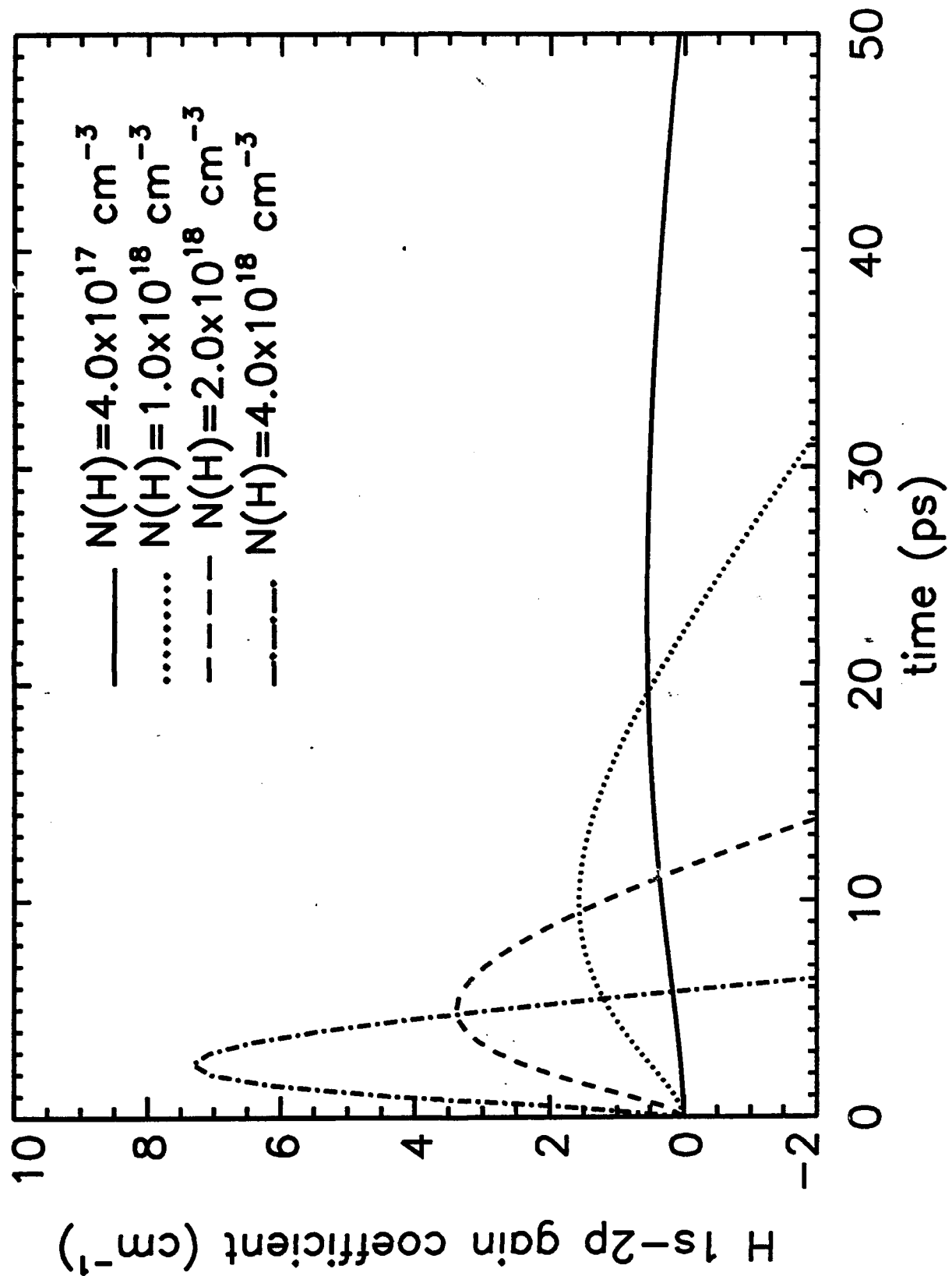


Figure 7

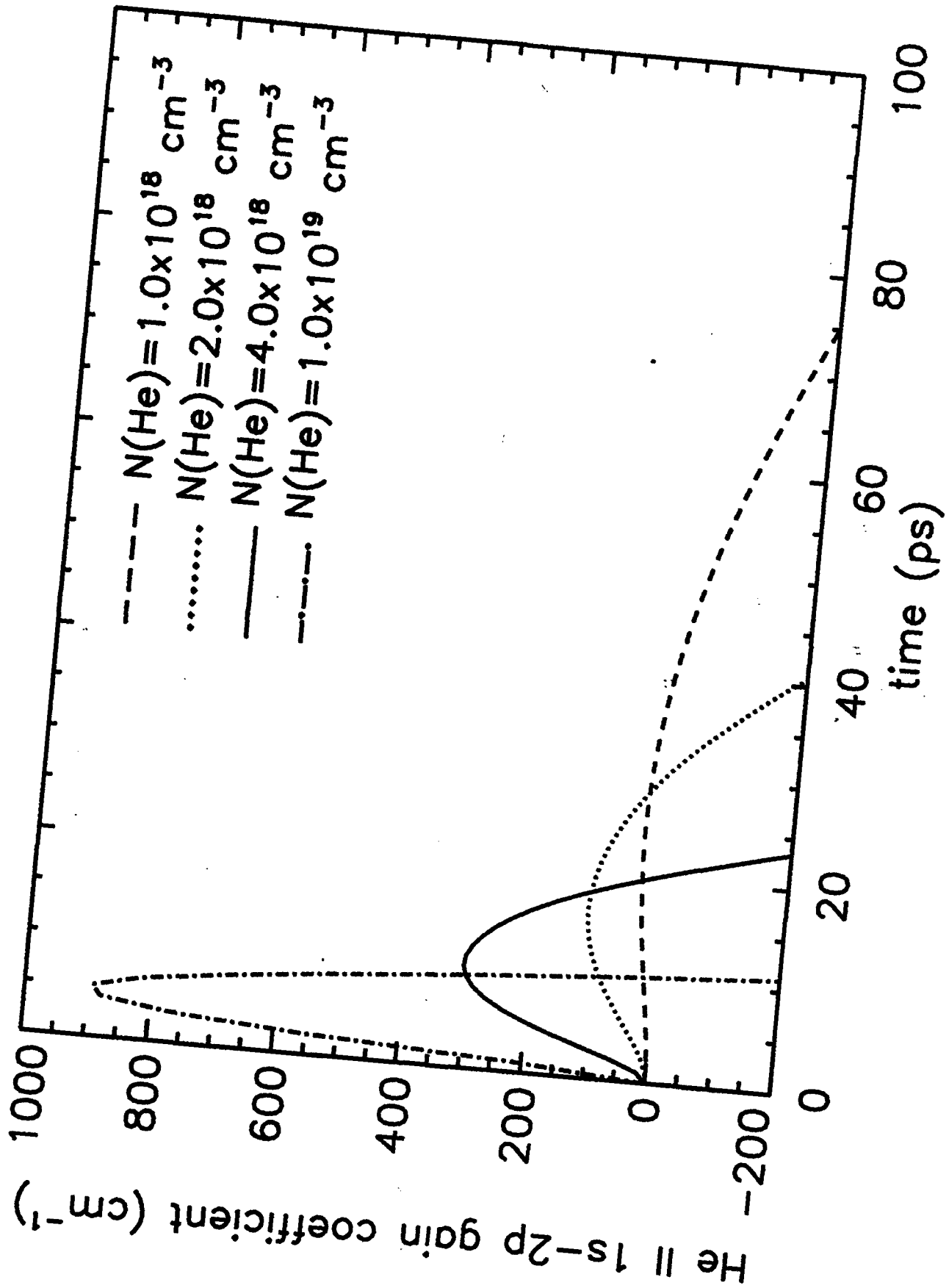


Figure 8

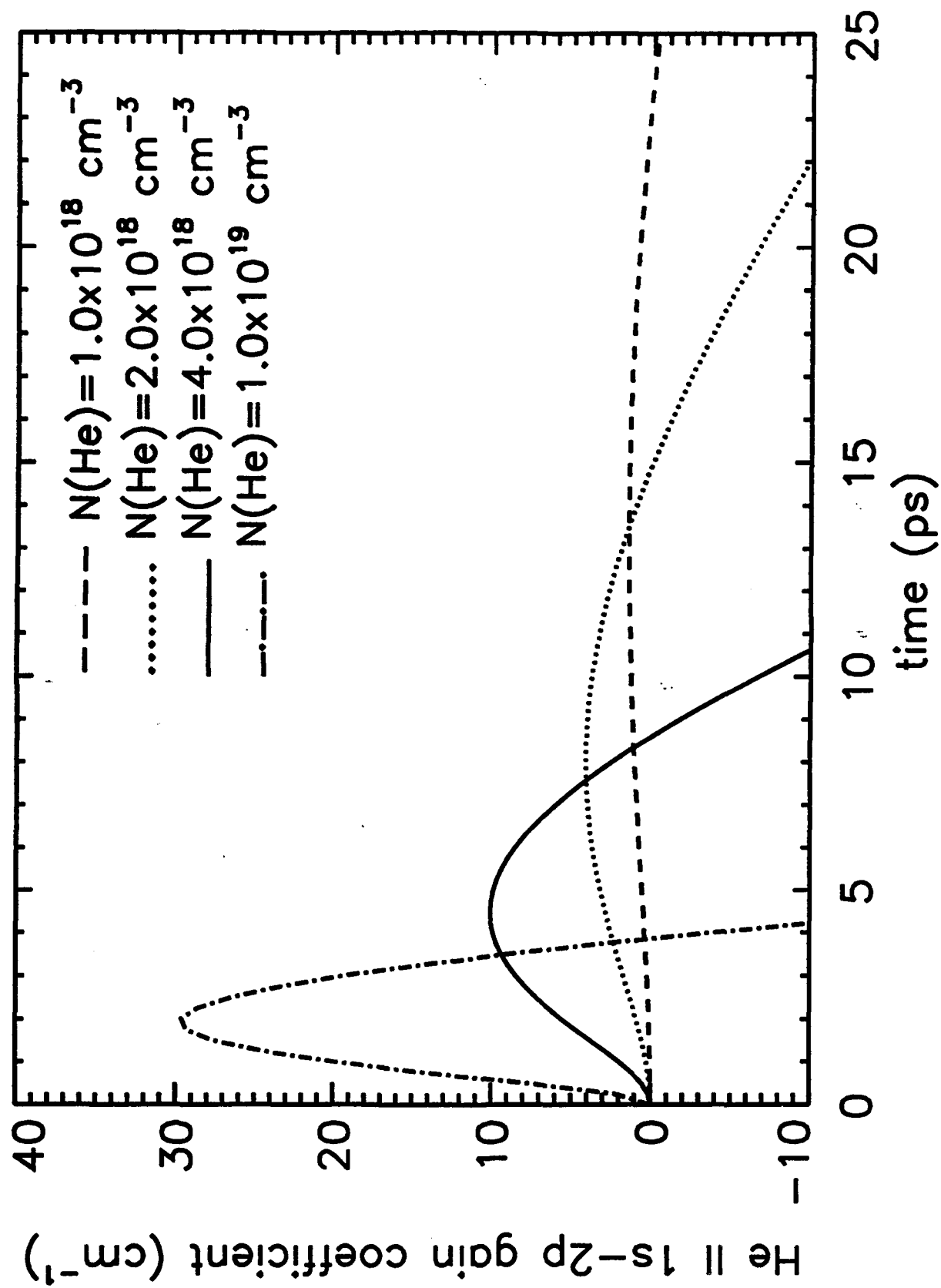


Figure 9

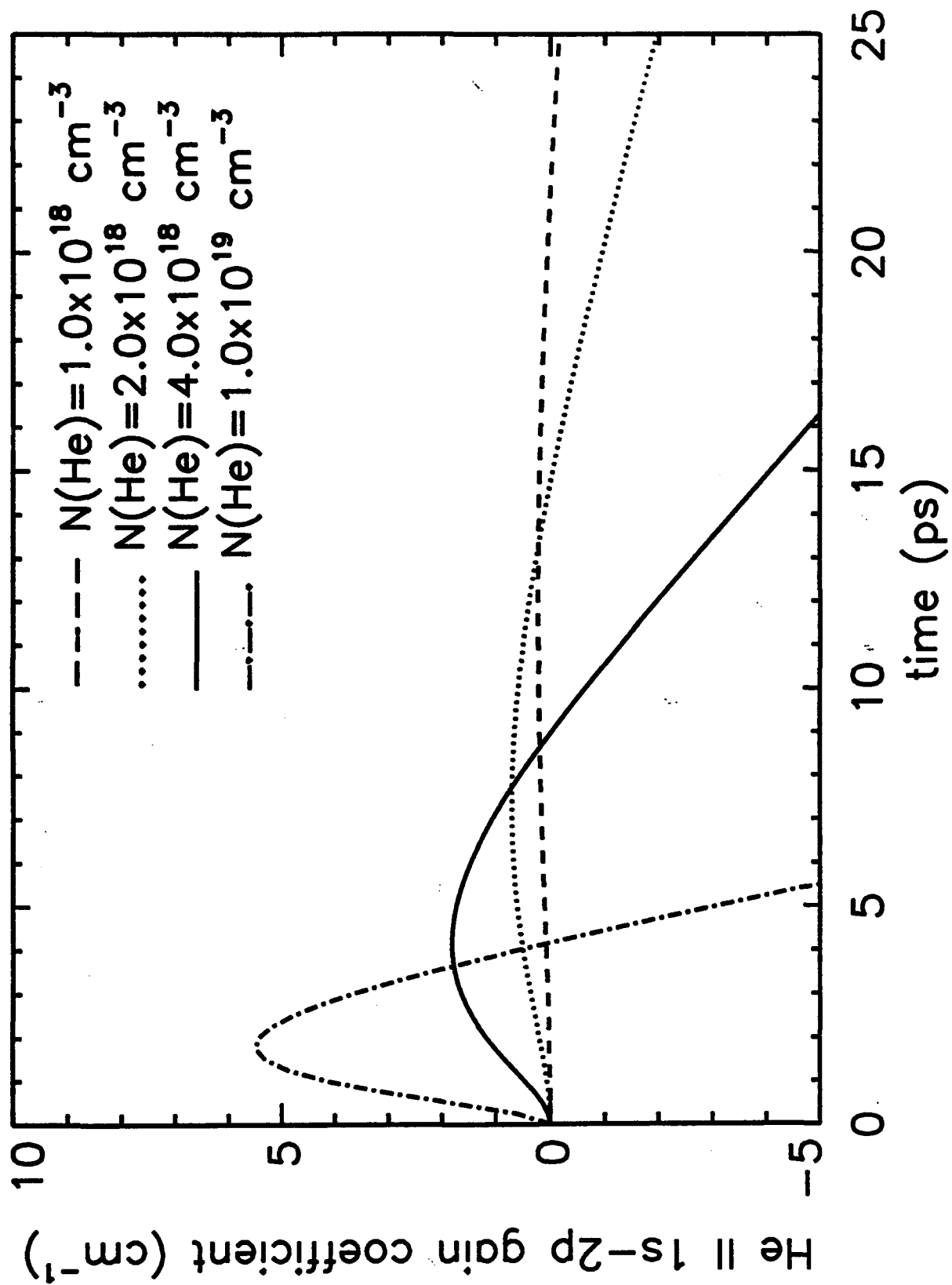


Figure 10

Ultra Short Laser Produced Al/Si Plasma

J. Davis, R. Clark and J. Giuliani

Plasma Physics Division

ABSTRACT

The x-ray emission from an ultra-short pulse laser produced aluminum/silicon plasma is investigated. A time history of the L- and K-shell line spectra, including the K_{α} lines and continuum radiation is presented for a laser intensity of 10^{17} watts/cm². The simulations are performed using a non-LTE radiation-hydrodynamics model coupled to a Helmholtz wave equation for P-wave polarization. A fraction of the absorbed energy is expended in the production of fast electrons, which are transported and deposited into the cold material. These electrons create K-shell vacancies which produce characteristic K_{α} line radiation. Analysis of this radiation provides information about the ionization of the target and the spectrum of the energetic electrons.

1. INTRODUCTION

The interaction of high powered pulsed lasers with planar targets has been the subject of intensive investigation for over three decades. The major emphasis of the research was focused on stabilizing the Rayleigh-Taylor (RT) instability for application to laser fusion experiments. Although interest remains high for the eventual control of the RT instability, a necessary criterion for the success of the laser fusion program, a number of other activities and technologies has emerged. One of these activities results from the development of techniques which makes it possible to produce ultra short pulse lasers with pulsewidths of tens to hundreds of femtoseconds and intensities in excess of 10^{18} watts/cm². This newly evolving technology is creating a number of innovative and exciting applications involving the interaction of ultra short pulse lasers with matter including x-ray lasers, laser produced solid density plasmas, subnanosecond spectroscopy, and the interaction of intense laser fields with atoms, molecules and energetic electron beams. The interaction of these intense lasers with planar targets makes it feasible to investigate solid state plasmas as a potential source of intense x-ray radiation in a relatively quiescent environment, since the target plasma remains nearly stationary during the initial burst of x-rays.

In this paper, we investigate the interaction of an ultra short pulse laser with a planar aluminum target, with the focus of the research directed toward characterizing the radiative properties and behavior of the

evolving plasma. The resulting radiation pulse represents a potentially useful source of x-rays for a variety of applications. In addition to the thermal plasma reservoir, there are groups of energetic electrons created in the absorption process that deposit their energy in the colder dense regions of the target producing inner shell transitions on a time scale of a few picoseconds. The mechanisms for the production and deposition of energetic electrons have recently been studied (Chen, Soom, Yaakobi, Uchida and Meyerhofer 1993) by making use of the resulting inner shell radiation. For example, a series of K_{α} lines is produced by resonance fluorescence in various ions of the target material. The relative strengths of these lines can be used to estimate ionic abundances in the vicinity of the energetic electron deposition as well as the characteristics of the fast electrons.

2. MODEL

2.1 Hydrodynamic Model

The basic hydrodynamic variables consisting of mass, momentum and total energy are transported in one dimension using a Lagrangian flux-corrected transport numerical scheme. The hydrodynamic equations solved are

$$\frac{D\rho}{Dt} = \frac{\partial\rho}{\partial t} + \frac{\partial(u\rho)}{\partial x} = 0,$$

$$\frac{D(u\rho)}{Dt} = -\frac{\partial P}{\partial x} + F_P,$$

$$\frac{D\epsilon_T}{Dt} = -\frac{\partial(uP)}{\partial x} + uF_P + \frac{\partial\epsilon_{source}}{\partial t},$$

$$\frac{\partial\epsilon_{source}}{\partial t} = \dot{\epsilon}_{rad} + \dot{\epsilon}_{laser} + \dot{\epsilon}_{con} + \dot{\epsilon}_{efast}$$

where ρ is mass density, u is velocity, P is pressure and ϵ_T is total energy. $\dot{\epsilon}_{rad}$, $\dot{\epsilon}_{con}$, $\dot{\epsilon}_{laser}$ and $\dot{\epsilon}_{efast}$ are the rates of energy gain (or loss) due to radiation, thermal conduction, laser deposition and fast electron deposition, respectively. The ponderomotive force, F_P , is given by

$$F_P = -\frac{\omega_{pe}^2}{16\pi\omega^2}\nabla E^2,$$

where ω is the incident laser frequency, ω_{pe} is the electron plasma frequency and E is the local electric field.

A single temperature approximation is employed, $T_e = T_i$, where

$$kT = \frac{\epsilon_T - \frac{1}{2}\rho u^2 - \epsilon_i}{\frac{3}{2}(n_e + \sum_m N_m)}$$

$$P = n_e kT_e + \sum_m N_m kT_i + P_F$$

where n_e is the electron density, ϵ_i is the ionization energy, N_m is the ion density of species m , and P_F is the Fermi pressure. The assumption of a single temperature breaks down in situations where the equilibration time is comparable with the heating time and the local average charge state is small. Near the critical surface, for example, the equilibration time condition is violated long before the peak of the laser pulse, but because of the local ionization (initially from multiphoton ionization), an acceptably small error in the electron temperature is incurred.

2.2 Atomic Model

The ionic populations in the plasma may be characterized by a set of atomic rate equations of the form

$$\frac{\partial f_{ikm}}{\partial t} = \sum_j (W_{jikm} f_{jkm} - W_{ijkm} f_{ikm}),$$

where f_{ikm} is the fractional population of atomic level i for species m in spatial zone k , and W_{jikm} is the net rate describing the transition from initial state j to final state i . An equation of this type is constructed for each of the atomic levels included in the model. The rate coefficients that are used to calculate the populating and depopulating rates, W_{jikm} , are calculated using various scattering techniques and the methods used in calculating the corresponding rate coefficients are summarized in Duston, Clark, Davis and Apruzese (1983).

Radiation emission from the plasma and its opacity are dependent on the local atomic-level population densities. Except for optically thin plasmas, however, the level populations depend on the radiation field, since optical pumping via photoionization and photoexcitation can produce significant population redistribution. Thus, the ionization and radiation transport processes are strongly coupled and must be solved self-consistently. In this model, an iterative procedure (Duston et al. 1983) is used, where level populations are calculated using the radiation field from the previous iteration, then using these populations to calculate a new radiation field until convergence is reached.

The prescription for multiphoton ionization follows the tunneling ionization theory of Ammosov, Delone and Krainov (1986), given by

$$W_{mp} = 1.61 \omega_{a.u.} \frac{Z^3}{n_{eff}^{4.5}} \left[10.87 \frac{Z^3}{n_{eff}^4} \frac{E_{a.u.}}{E} \right]^{2n_{eff}-1.5} e^{-2Z^3 E_{a.u.}/3n_{eff}^6 E}$$

where $\omega_{a.u.} = 4.1 \times 10^{16} s^{-1}$ is the atomic unit of frequency, $E_{a.u.} = 5.1 \times 10^9 V/cm$ is the atomic field strength, and the effective quantum number n_{eff} is obtained by hydrogenic scaling

$$n_{eff} = \frac{Z}{(U_i/U_H)^{1/2}}$$

where $U_H = 13.6 eV$ is the ionization potential of hydrogen, U_i is the ionization potential of the critical electron orbit, and Z is the residual charge seen by the electron. Multiphoton processes produce some

initial ionization of the plasma, but become unimportant compared with collisional ionization as the plasma is heated.

The atomic model for aluminum used in this calculation consists of the ground states and 118 excited levels through neutral aluminum, including structure up to N=10 for H-like, and to N=9 for He-like and Li-like aluminum. The atomic model for silicon consists of the ground states and 65 excited levels. Ionization lowering is accounted for by means of an ion sphere model; the bound-free radiation is limited from states which merge with the continuum. Radiation transport is carried out using a probability-of-escape formalism which is described in Apruzese (1981 and 1985).

2.3 Laser deposition model

The absorption of a laser pulse obliquely incident on a planar target is calculated by solving the Helmholtz wave equation. In this way, the incident, reflected and transmitted waves are self-consistently characterized in each spatial zone in the medium. The conductivity is obtained from the Cauble et. al. (1987 and 1990) model. The conductivity is complex, with

$$\sigma = \frac{n_e e^2}{m_e} \frac{1}{\nu - i\omega} = \left(\frac{\omega_{pe}^2}{\nu^2 + \omega^2} \right) \frac{\nu + i\omega}{4\pi} = \frac{i\omega}{4\pi} (1 - \epsilon')$$

where ν is the collision frequency and ω is the laser frequency.

The Helmholtz equations for the electric and magnetic fields can be written

$$\nabla^2 \vec{E} + \frac{\omega^2}{c^2} \left(1 + i \frac{4\pi\sigma}{\omega} \right) \vec{E} = \nabla^2 \vec{E} + \frac{\omega^2}{c^2} \epsilon' \vec{E} = 0$$

$$\nabla^2 \vec{B} - \frac{\nabla \epsilon'}{\epsilon'} \times (\nabla \times \vec{B}) + \frac{\omega^2}{c^2} \epsilon' \vec{B} = 0$$

where ϵ' is the plasma dielectric function. For S-polarization, take $\vec{E} = E_s(x, y)\hat{e}_z = E_s(x)\hat{e}_z e^{-i\omega \sin\theta_0 y/c}$. In this case, it is convenient to use the Helmholtz equation for \vec{E} , which reduces to

$$\frac{\partial^2 E_s(x)}{\partial x^2} + \frac{\omega^2}{c^2} [\epsilon' - \sin^2\theta_0] E_s(x) = 0.$$

For P-wave polarization, it is more convenient to solve for the magnetic field, $\vec{B} = B_s(x, y)\hat{e}_z$, and the corresponding Helmholtz equation can be written

$$\frac{\partial^2 B_s(x)}{\partial x^2} - \frac{\partial \ln \epsilon'}{\partial x} \frac{\partial B_s(x)}{\partial x} + \frac{\omega^2}{c^2} [\epsilon' - \sin^2\theta_0] B_s(x) = 0.$$

A Runge-Kutta numerical scheme is employed to solve the appropriate Helmholtz equation. An adaptive gridding is used to resolve the fields in the vicinity of the critical surface. The computational mesh used for the solution of the fields is much finer than that used for the hydrodynamics and radiation

transport; logarithmic interpolation is employed to obtain the electron density and collision frequency from the hydrodynamic computational mesh.

2.4 Energetic electron transport

A fixed fraction of the laser energy deposited in each spatial zone (10 percent in the present calculation) is assumed to be expended in the production of energetic electrons. These fast electrons are assumed to be monoenergetic (at an energy between 4.0 and 10.0 keV). This assumption is made to simplify the interpretation of the resulting data; a Maxwellian (or an arbitrary energy distribution) could be employed in the model. The energetic electrons are transported, and subsequently deposit their energy in the plasma, giving rise to local heating and inner-shell vacancies.

At sufficiently high electron energies, the Bethe theory is reasonably accurate. Then the fast electron stopping power can be written in the Bethe-Bloch form (as given in Powell 1976)

$$\frac{\partial E}{\partial x} = -\frac{2\pi e^4 n_i}{E} \left[Z_B \ln\left(\frac{1.16E}{\chi_{av}}\right) + Z_F \ln\left(\frac{1.16E}{\chi_o}\right) \right]$$

where χ_{av} is an average ionization potential, χ_o is an effective potential related to the electron plasma frequency, and Z_B and Z_F are the effective number of bound and free electrons per ion. The continuous slowing down model breaks down when quantum transitions are of the same order in energy as the beam.

2.5 K_α radiation model

The K-shell vacancies which are created are rapidly filled by either Auger decay (radiationless cascade) or resonance fluorescence (valence electron fills vacancy with the emission of K_α radiation). The energy-dependent K_α production rate is calculated for each aluminum ionization stage in each spatial zone, from Al I (neutral aluminum) through Al IX (boron-like aluminum), and for the corresponding silicon ionization stages. The K-shell vacancy cross sections for aluminum and silicon were obtained from the calculations of Blaha (1992), and represent a small fraction of the total stopping power. From threshold to about 10keV, the energy dependence of these cross sections can be approximated by a simple slowing-down approximation

$$\sigma(E) = \frac{C}{(E \chi_k)} \ln\left(\frac{E}{\chi_k}\right)$$

where C for aluminum is equal to $9.5 \times 10^{-14} \text{ cm}^2/\text{eV}^2$ and χ_k is given in Table I for each ionized state of aluminum. The fluorescence/Auger decay branching ratios (taken from Duston et al. 1983) vary with ionization stage, and are typically about 5 percent. The K_α line widths are determined from the inverse lifetimes. The K_α lines for Al I-IV (and for Si I-V) lie so close together in energy that they appear spectroscopically as a single line, whereas those of Al V-IX (and Si VI-X) are sufficiently separated that they can be resolved.

Table I lists by ion the K_{α} energy, the resonance fluorescence/Auger decay branching ratio, and the potential used to fit the K-shell vacancy cross section for aluminum. A similar set of energies and branching ratios is used for the silicon K_{α} radiation.

TABLE I: K_{α} Parameters for Aluminum

Ion	K_{α} Energy	$K_{\alpha}/\text{vacancy}$	χ_k
Al I	1486.99 eV	0.0330	1600 eV
Al II	1487.52 eV	0.0460	1630 eV
Al III	1488.24 eV	0.0450	1660 eV
Al IV	1488.95 eV	0.0434	1690 eV
Al V	1499.58 eV	0.0479	1750 eV
Al VI	1511.64 eV	0.0522	1810 eV
Al VII	1525.40 eV	0.0619	1870 eV
Al VIII	1540.37 eV	0.0700	1930 eV
Al IX	1557.01 eV	0.0623	2000 eV

3. RESULTS

3.1 Aluminum Target

An ultrashort-pulse laser (0.22 psec FWHM duration Gaussian with no prepulse) was assumed to be obliquely incident (30 degrees from the normal) on solid density aluminum and layered aluminum/silicon targets. The peak power was 1.0×10^{17} W/cm² at a wavelength of 0.26 μ . Figure 1 shows the time dependence of the incident laser power, the absorption fraction (absorbed energy relative to the total incident energy) assuming P-wave deposition, and the temperature at the critical surface.

The reflectivity varies from about 40 to 70 percent during the laser pulse, and is about 50 percent near peak incident power. In the case of layered aluminum/silicon targets, the details of the absorption may be different, but the laser deposition features which are important to this discussion (reflectivity, absorption fraction, etc.) will be approximately the same. The energy distribution history is plotted in Figure 2 for a solid aluminum target. Initially most of the energy in the target is thermal. As the laser energy is deposited, the thermal and ionization energies rise. Kinetic energy increases rapidly as the ablation process becomes important, and is comparable with the thermal energy at the peak of the laser pulse. Because the timescale is so short, the radiation energy is about three orders of magnitude less than the thermal energy at 0.40 picoseconds. At late times, the plasma expands, cools and recombines. Eventually, much of the ionization energy will be radiated away (radiative recombination). Thus, the x-ray radiation pulse from the target will

be much longer than the incident laser pulse. The energy histories for the layered target configurations closely approximate Figure 2.

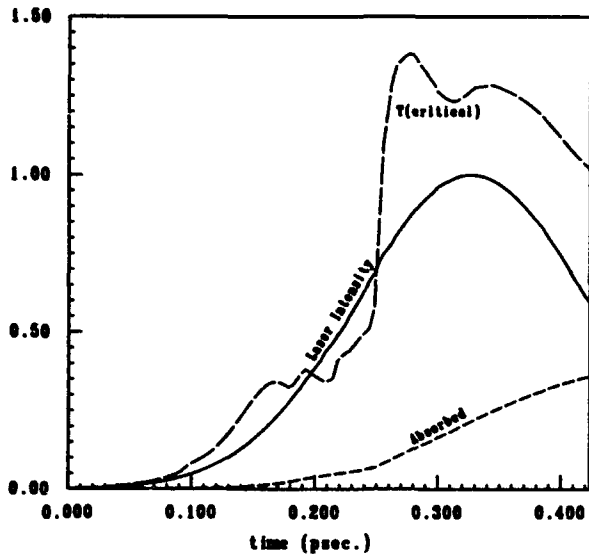


Figure 1. Incident laser power normalized to the peak of the laser pulse (10^{17} W/cm^2), absorption fraction, and temperature at the critical surface in tens of keV are shown as functions of time for P-wave deposition.

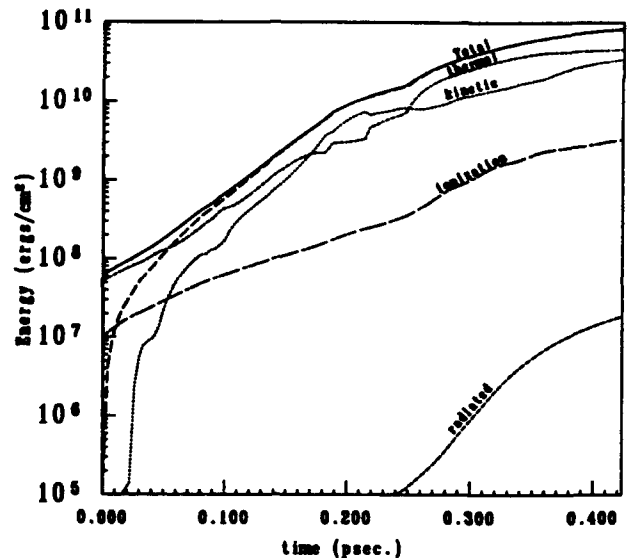


Figure 2. Energy history for a 10^{17} W/cm^2 pulse incident on a solid aluminum target. The total energy in the plasma is shown, as well as the thermal, kinetic, ionization (and excitation) and radiated energies.

Figure 3 shows the electric and magnetic fields and the local energy deposition rate in the target near the peak of the laser pulse (0.30 picoseconds) for an aluminum target. The laser pulse is assumed incident from right to left. The fields are averaged over an optical cycle, and normalized with respect to the amplitudes of the incident electric and magnetic fields. The magnetic field is plotted on a linear scale. However, the electric field becomes so large near the critical surface, that the logarithm (\log_{10}) of the field is plotted. The location of the critical surface, i.e. where the incident laser frequency is equal to the plasma frequency ($\omega = \omega_p$) is represented as R_{crit} . The density is plotted in a stepwise manner to show the spatial resolution of the hydro mesh.

In the absence of an energetic electron beam, the temperature profile would be mostly dominated by thermal conduction from the laser deposition region and would exhibit a rapid decay into the cold aluminum. The density is nearly constant behind the blowoff, although a small disturbance (a rarefaction and a weak shock) can be seen near $x = 1.0 \mu$ in Figure 4 due to the fast electron heating. Radiative losses are the

greatest near $x = 2.0 \mu$ where the plasma is hot. A secondary cooling peak occurs at about 0.90μ , but is not in the range of the plot.

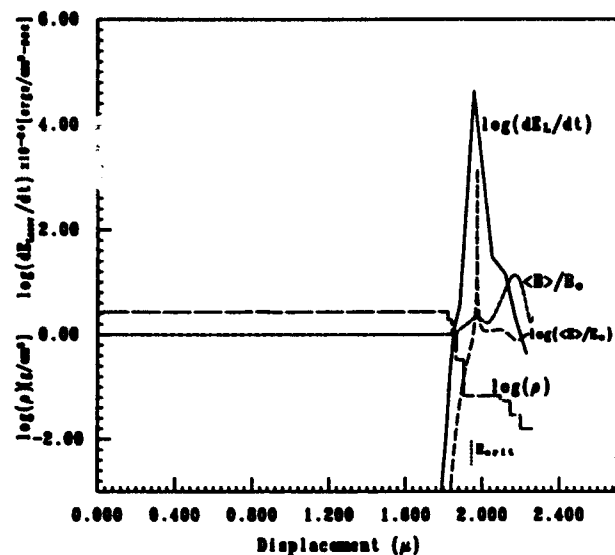


Figure 3. Energy Deposition into an Aluminum Target. The rate of energy deposition into the target dE_L/dt is plotted, and the location of the critical surface R_{crit} is shown. The local electric and magnetic fields, averaged over an optical cycle, are shown normalized to the amplitude of the incident fields, E_0 and B_0 . Mass density ρ is plotted in a stepwise manner.

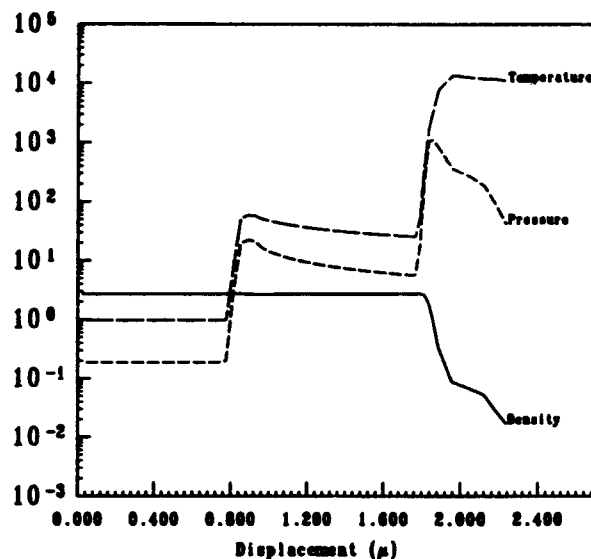


Figure 4. Hydrodynamic profiles in the target at 0.30 picoseconds. Mass density ρ [g/cm^3], temperature T [eV], pressure P [$ergs/cm^3 \times 10^{-12}$], and radiative cooling dE_R/dt [$ergs/psec - cm^3 \times 10^{-14}$] are plotted as functions of position.

The laser (dE_L/dt) and fast electron (dE_F/dt) energy deposition profiles are represented in Figure 5. The local K_α powers by ionization state produced by the deposition of fast electrons are also shown, including neutral (I) through boron-like aluminum (IX). Most of the neutral and magnesium-like aluminum K_α radiation originates in the cold target region lying between about 1.0μ and 1.7μ . Intermediate-ion K_α radiation (from fluorine-like through sodium-like aluminum) originates in the hot laser-deposition region ($x \approx 1.8 \mu$) and in the warm fast-electron heated region ($x \approx 0.9 \mu$). The K_α radiation from highly ionized aluminum (oxygen-like aluminum and above) comes mostly from the hot laser deposition region.

The instantaneous distribution of K_α radiation is correlated with the local atomic populations. At early times (before significant ionization can take place) only K_α -I and K_α -II is seen. Most of the K_α from highly ionized aluminum is created at intermediate times, near and shortly after the peak of the laser pulse, when

the plasma reaches maximum ionization. At later times, the plasma cools and recombines. Even spatially integrated K_{α} radiation can give a wealth of information about the instantaneous state of the plasma.

The instantaneous spatially integrated x-ray emission spectrum for the K-shell and K_{α} lines is plotted as a function of photon energy at 0.30 picoseconds (near the peak of the laser pulse) in Figure 6. The spectral lines are identified on the figure. The most distinguishing feature of the spectrum is the series of K_{α} lines generated by the energetic electrons. The K_{α} lines from the four lowest aluminum ionization stages (K_{α} -I through K_{α} -IV) lie so close together in energy that they appear in the spectrum as a single line; the remaining K_{α} lines are well resolved. The K_{α} I-IV line is prominent in the spectrum, and is comparable in intensity with the He- α line.

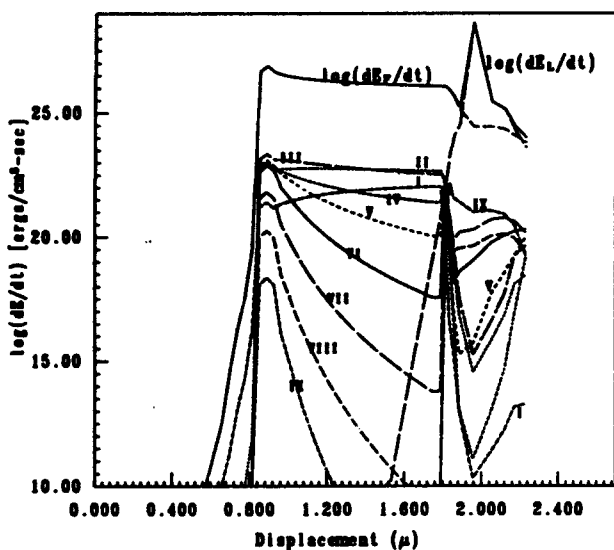


Figure 5. Energy deposition at 0.30 picoseconds for P-polarization. The logarithm of the rate of laser energy deposition dE_L/dt and fast electron energy deposition dE_F/dt [$\times 10^{10} \text{ kW/cm}^2$] are plotted with the K_{α} powers for various ionized states of aluminum produced by the deposition of fast electrons. They include neutral (I) through boron-like aluminum (IX).

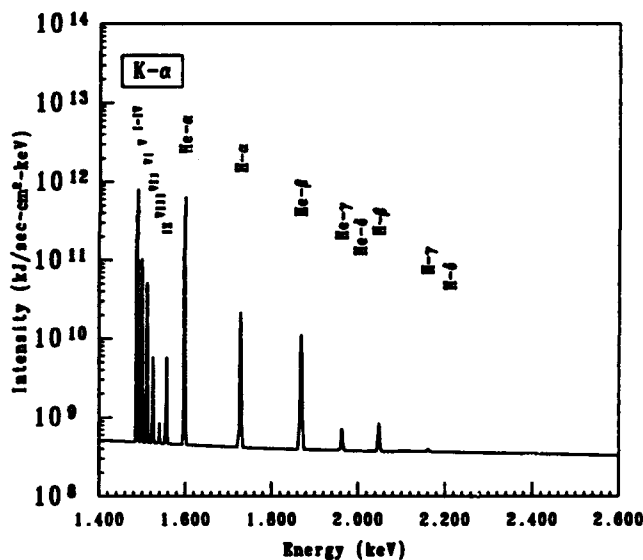


Figure 6. Emission spectrum at 0.30 picoseconds for an aluminum target, showing magnitudes of the K_{α} and K-shell lines. The He- α line is comparable to the neutral K_{α} line of aluminum.

The relative intensities of the lines reflect the local atomic populations which the energetic electrons encounter. As Figure 5 illustrates, high states of ionization are encountered in the blowoff plasma, and low ionization states are encountered elsewhere. Al II and Al III are the most abundant ion species in the cold target, and neutral aluminum is down in abundance by about an order of magnitude. Most of the fast

electrons are generated near the critical surface; since the stopping power varies with electron energy as $\ln(E)/E$, K-shell vacancies are created more efficiently about a micron into the target, when the electrons have slowed down (Al II through Al V dominates in this region). Finally, Al IX dominates the hot blowoff region; the lower ionization states are substantially depleted. In the simulations, K_{α} transitions for Al X and higher are not considered. The result of these considerations is seen in the relative intensities of the K_{α} lines in Figure 6.

3.2 Layered Silicon/Aluminum Target

While the relative intensities of the K_{α} lines can provide detailed information about atomic populations, it is difficult to use this knowledge in the differentiation of fast electron phenomena from laser absorption effects. However, the use of multiple materials in the target with layers of varying thicknesses provides additional spectral information. The range of energetic electrons in the target can be determined directly from such experiments, and the electron energy distribution function can thus be inferred. In addition, it may be possible to make quantitative measurements of laser absorption as a function of position in the target, and to verify assumptions regarding multiphoton processes, etc.

A series of layered target simulations was carried out, where the initial conditions were essentially identical with the aluminum slab target described above (0.22 psec FWHM duration Gaussian pulse incident at 30 degrees from the normal with peak power 1.0×10^{17} W/cm² and a wavelength of 0.26 μ). In the first case, the laser was incident on a 0.10 μ silicon layer coating a solid density aluminum substrate. The energetics of the deposition, the energy history and the hydrodynamic response of the target, and the production and deposition of energetic electrons in the target are approximately the same as for the case of the plain aluminum target, as shown in Figures 1 through 5. Naturally, there are differences in the details, because silicon has a different solid density and different ionization potentials, etc. However, because aluminum and silicon are adjacent elements on the periodic table, these differences are not large. The most significant difference between the simulations is the resulting radiation, particularly the K-shell emission.

Figure 7 shows the K-shell emission spectrum at the peak of the laser pulse for the case of a 0.10 μ silicon coating on an aluminum target. As in the plain aluminum case discussed above, the fast electrons are assumed to be monoenergetic at 10 keV. Now there are two sets of K_{α} radiation in evidence. Clearly, the aluminum plasma is not as hot as in Figure 6; aluminum K-shell radiation is completely absent except for the K_{α} V line, and the K_{α} V line is almost two orders of magnitude down from the I-IV line. However, the silicon radiation suggests that the outermost 0.10 micron of plasma is hot. Some care must be taken in the identification of the lines, because certain aluminum lines are almost coincident with silicon lines. The Rydberg series lines from H- and He-like silicon are observed; these result from the decay of nP states ($n \leq 5$) to the 1s orbitals. The silicon K_{α} radiation apparently comes from two distinct sources. The K_{α} I-V line originates in cooler plasma (behind the critical surface), and the VII through X lines come from the

hot region just ahead of the critical surface. These regions correspond to those described in Figure 5. At this time, the back edge of the silicon layer just barely extends into the cool region extending from about 1.2μ to 1.8μ .

If the fast electrons have less energy, their range is correspondingly decreased, and the plasma just behind the critical surface becomes hotter (the electron energy is deposited in a smaller volume). Figure 8 shows the K-shell emission spectrum for an identical simulation, except that the fast electron energy is assumed to be 4.0 keV. The aluminum still does not get hot enough to produce thermal radiation in the K-shell; however, the K_{α} signature is considerably different. The K_{α} V and VI lines are nearly as strong as the I-IV line, and the VII line is almost an order of magnitude less intense. The I-IV line is substantially less intense than in Figure 7. The silicon emission is also altered, but in a more subtle way. All of the silicon K_{α} lines are more intense, because more fast electrons are being stopped in the silicon layer. In addition, the relative brightness of the K_{α} VI line is increased, since the plasma immediately behind the critical surface is warmer.

The local K_{α} powers by ionization state produced by the deposition of fast electrons for the present case is plotted as a function of position in the target in Figure 9. The portion of the target from 1.2 to 2.2 microns is shown, since the fast electrons have substantially reduced range at 4.0 keV. The plasma at and ahead of the critical surface looks qualitatively similar to the corresponding region in Figure 5. The details are different because the fast electron deposition is altered and because the material is silicon rather than aluminum. There is substantial production of silicon K_{α} IX and X in the hot plasma. However, deeper into the target (between about 1.6 and 1.8 microns), the plasma is qualitatively different. It is hotter because of the reduced energetic electron range, and the ionization state is higher. The fast electrons are creating K-shell vacancies in more highly ionized material (predominately aluminum). There are strong gradients in the K_{α} powers near 1.78 microns, which is at the aluminum/silicon interface. The plot illustrates that the actual K_{α} production is more complicated than the spectra suggest. There are at least six regions in the target plasma where the ionization physics is distinct. Deep in the target, the (aluminum) plasma is cold and essentially unionized. Between about 1.6 and 1.78 microns the (aluminum) plasma is warm (of the order 100 eV), and aluminum II-VI predominates. Sandwiched between this and the critical surface region, the plasma is also of the order 100 eV, and silicon IV-VI is most prevalent. Near the critical surface, the silicon is hot and dense; silicon VIII-X predominates. Ahead of this region (near 1.9 microns) the density is somewhat lower and silicon IX-X is most abundant. Since we only consider K_{α} lines of silicon through boron-like, the plot contains no information about silicon XI-XV. Finally, near 2.2 microns, intermediate ionization states of silicon dominate, since the density is low and the plasma is far from equilibrium. In this way, the fast electron energy spectrum can be estimated. The layer thicknesses can be varied to give additional information about the range of the electrons. The results of such simulations will be incorporated into a subsequent paper.

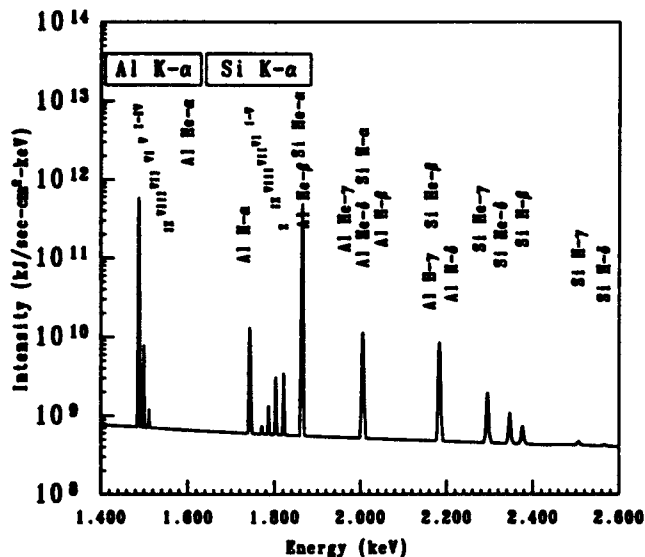


Figure 7. Emission spectrum at 0.30 picoseconds for an aluminum target with an 0.10μ silicon coating. The K-shell (including the K_{α} lines) of aluminum and silicon are shown. The fast electrons are assumed to be monoenergetic at 10 keV.

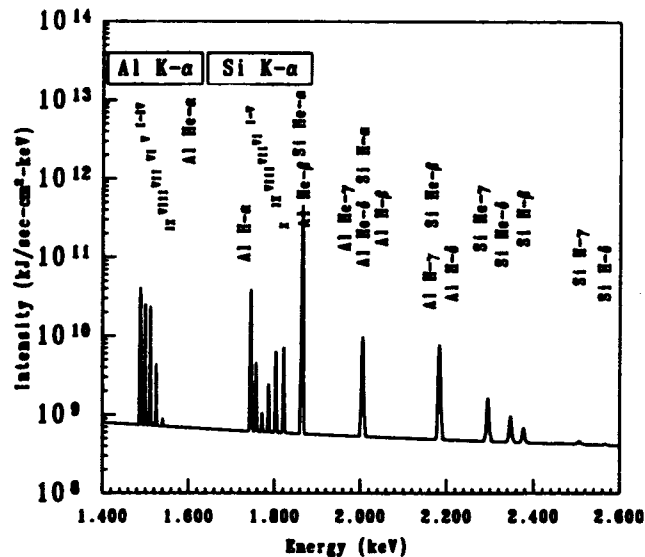


Figure 8. Emission spectrum at 0.30 picoseconds for an aluminum target with an 0.10μ silicon coating. The fast electrons are assumed to be monoenergetic at 4 keV.

The use of this diagnostic is further illustrated by comparing the spectra from aluminum/silicon and silicon/aluminum targets. Figure 10 shows the K-shell emission for the case of a 0.10μ aluminum coating on a silicon substrate. The laser characteristics are the same as for the previous cases, and the energetic electrons are taken to be at 4.0 keV. Now aluminum K-shell radiation (the Rydberg series lines from H- and He-like aluminum) is in evidence, and silicon K-shell radiation is absent except for the K_{α} lines. The aluminum H- α line is situated just below silicon K_{α} sequence in energy (and can easily be mistaken for the first line of the sequence); it is at least an order of magnitude more intense than the silicon K_{α} I-V line. The K_{α} lines from higher stages of ionization in silicon (VI and VII) fall off rapidly. This result is in contrast with the silicon-on-aluminum spectrum, where the first three K_{α} lines were comparable in intensity. This implies that the silicon-on-aluminum plasma is slightly warmer behind the aluminum/silicon interface. This can be explained by the different energetic electron stopping powers of aluminum and silicon and by the different electrical conductivities of the species which can produce variations in the laser deposition.

The aluminum K_{α} lines are all comparable in intensity; however, the K_{α} VIII line is weak. As before, this implies that the radiation is coming from two distinct regions. The K_{α} I-VII is coming from a warm region just behind the critical surface. The K_{α} IX comes mainly from the hot plasma at and ahead of the

critical surface. The spectra in Figures 8 and 10 thus convey similar information. The differences between them illustrate the complications that arise in interpreting spectral data.

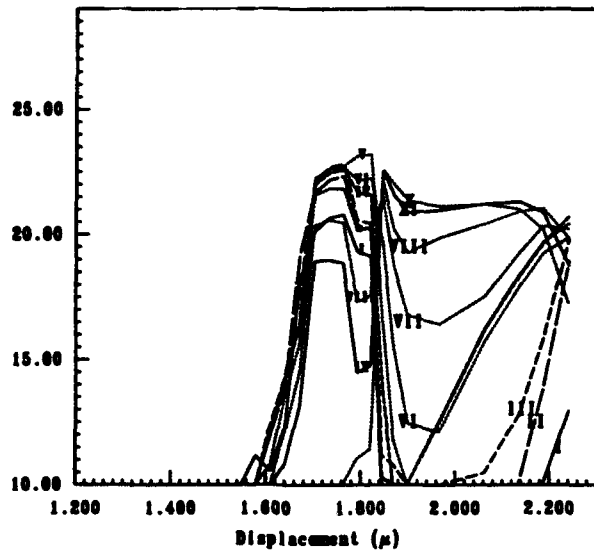


Figure 9. K_{α} powers for various ionized states of aluminum and silicon produced by the deposition of fast electrons. They include neutral (I) through boron-like aluminum (IX), and neutral through boron-like silicon (X).

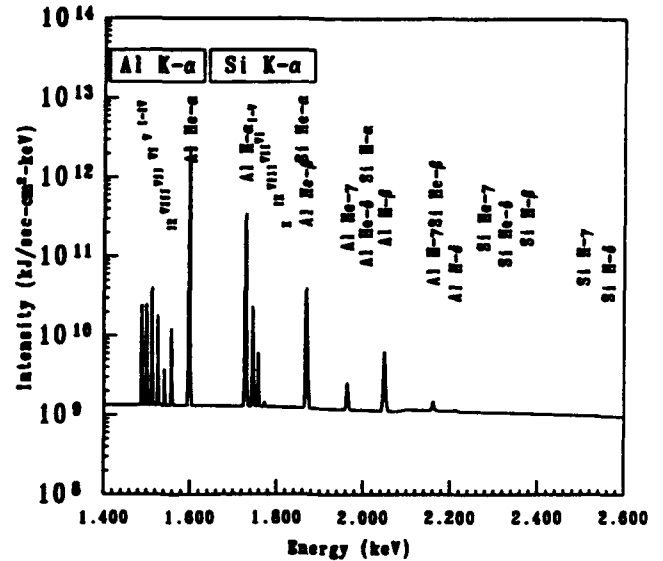


Figure 10. Emission spectrum at 0.30 picoseconds for a silicon target with an 0.10μ aluminum coating. The fast electrons are assumed to be monoenergetic at 4 keV.

4. CONCLUSIONS

The purpose of this investigation was to simulate the radiation hydrodynamics of an ultrashort pulse laser produced plasma and to study how the emitted x-rays could provide information about the energy deposition in the target, the production and transport of energetic electrons, and the resulting ionization of the plasma. The model which was used included a relatively detailed treatment of the atomic populations and radiation. The laser deposition was performed in a self-consistent manner by solving the appropriate Helmholtz equation. The treatment of the energetic electrons incorporated a number of prescriptions (production rate and energy distribution), but it provided for the self consistent transport of the electrons and the production of K-shell vacancies. One aspect of the calculation that needs improvement is the spatial resolution in the vicinity of the critical surface. Since K_{α} radiation is produced almost entirely by

the energetic electrons, these inner shell K-lines are particularly useful in providing information on energy transport due to fast electrons. However, the ratios of the K_{α} lines reflect the local atomic populations where the electrons produce K-shell vacancies. It is challenging to accurately determine the electron energy spectrum from this data alone. The details of the laser deposition and other factors which can alter the density and temperature profiles (and the local ionization of the plasma) can also affect the line ratios. The deposition is controlled by the local electrical conductivity, and progress continues to be made by a number of researchers in developing a satisfactory conductivity model for the conditions encountered in these plasmas. The use of very thin multiple material layers (as has been explored by Chen et. al. 1993) is one way to provide additional information about the ionization of the plasma as a function of position in the target, and thus distinguish between these factors. It is hoped that the analysis of the dynamics of layered targets contained in the last section, although far from exhaustive, proves useful to experimentalists in interpreting their data. We also investigated the possibility of plasma conditions being generated in the target that are conducive to the creation of population inversions. For relatively high laser intensities (S-wave deposition at $3 \times 10^{17} W/cm^2$, for example), temperature and density profiles in the blowoff plasma have tentatively been found to support inversions in a number of upper states of lithium-like aluminum. The most favorable conditions seem to occur for electron densities of the order $10^{20} cm^{-3}$. These results will be presented and discussed elsewhere.

ACKNOWLEDGMENTS

We would like to thank Dr. P. Kepple for making the atomic data base available, and Dr. R. Cauble for providing assistance with the electrical resistivity. We would also like to acknowledge useful discussions with Drs. H. Milchberg and D. Meyerhofer.

REFERENCES

- AMMOSOV, M. V., DELONE, N. B. and KRAINOV, V. P. 1986 *Zh. Eksp. Teor. Fiz.* **91**, 2008.
- APRUZESE, J. P. 1981 *J. Quant. Spect. Rad. Transf.* **25**, 419.
- APRUZESE, J. P. 1985 *J. Quant. Spect. Rad. Transf.* **34**, 447.
- APRUZESE, J. P., DAVIS, J., DUSTON, D. and CLARK, R. 1984 *Phys. Rev. A* **29**, 246.
- BLAHA, M. 1992 *Private communication*.
- CAUBLE, R. and ROZMUS, W. 1987 *J. Plas. Phys.* **37**, 405.
- CAUBLE, R., ROGERS, F. J. and ROZMUS, W. 1990 *SPIE* **1229**, 211.
- CHEN, H., SOOM, B., YAAKOBI, B., UCHIDA, S. and MEYERHOFER, D. D. 1993
Phys. Rev. Lett. **70**, 3431.
- DUSTON, D., CLARK, R. W., DAVIS, J. and APRUZESE, J. P. 1983 *Phys. Rev. A* **27**, 1441.
- MILCHBERG, H. M. and FREEMAN, R. R. 1989 *J. Opt. Soc. Am. B* **6**, 1351.

Short-pulse Driven Selenium

X-ray Lasers

K. G. Whitney, A. Dasgupta, and P. E. Pulsifer

Plasma Physics Division

Abstract: The influence of intense picosecond heating and time dependent ionization on the population dynamics of Ne-like selenium is investigated. We find that highly non-equilibrium plasma conditions and a large gain coefficient $> 600 \text{ cm}^{-1}$ can be generated for the $J=0-1$ line at 182 \AA at KrF laser intensities $> 3 \times 10^{16} \text{ W/cm}^2$. Thus, the observation of x-ray lasing at or near the critical surface of a KrF short-pulse, laser driven plasma appears feasible. Its observation would provide important tests of theoretical models for laser absorption, transient ionization, and x-ray laser pumping.

Early in their development, it was conjectured that high power, picosecond pulsed lasers could become useful table-top drivers for x-ray lasers.¹ A number of different schemes for generating population inversions in the plasmas heated by picosecond or subpicosecond lasers were then proposed.^{2,3} In this letter, we present the results of calculations that demonstrate the feasibility of generating large transient population inversions within the neon-like ionization stage of selenium using short-pulse picosecond lasers. These inversions are large enough to produce a saturated amplified spontaneous emission (ASE) from a plasma ≤ 1 mm in length. These x-ray laser experiments could be carried out with 1 to 10 picosecond KrF laser pulses heating a pre-formed selenium plasma at or near the critical surface. The use of selenium in these experiments has two advantages. One, neon-like selenium x-ray lasers have already been operated in long-pulse (~ 500 ps) generated plasmas,⁴ and a number of their properties have been well studied experimentally.^{5,6} Two, fairly comprehensive models of their population dynamics have been constructed and benchmarked against experimental observations;^{7,8} one⁸ is used in obtaining the calculational results described in this letter.

Short-pulse generated plasmas are also of general interest as picosecond-pulsed sources of kilovolt x rays.⁹ Experimental observations, in this case, clearly indicate the need to rapidly heat a pre-formed plasma in order to generate the maximum number of x rays. The calculations we present support this observation. The hydrodynamic expansion of blowoff plasmas generally occurs on the order of nanosecond time scales; thus, the picosecond heating and ionization of a pre-formed selenium plasma can initially be studied by ignoring the effects of hydrodynamic expansion. For this purpose, we utilized the hot-spot model described earlier¹⁰ to determine the ionization response of selenium to picosecond heating. The selenium atomic model in this calculation consists of the hydrogenic lumped state model described in Ref. (11), to which the neon-like and fluorine-like structure, which is described in Ref. (8), was added. In this model, a full description is given of the transient excitation and ionization of all 26 $n=3$ states in the neon-like ionization stage from which x-ray lasing has been observed. Specifically, lasing was seen in two $J=0-1$ and two $J=2-1$ $3p$ to $3s$ transitions. However, at the plasma density of our problem, which will correspond roughly to the ion density of a KrF laser critical surface, the $J=2-1$ transitions cannot be inverted and show no gain even in transient ionization. The $J=0$, $3p$ states, on the other hand, are strongly populated from both the ground state and from the $J=1$, $3d$ states

due to the large monopole and dipole excitation rates from the ground state to both the $J=0$, 3p and $J=1$, 3d states, respectively. Hence, during transient excitation, a large population inversion can be established between the $J=0$, 3p and $J=1$, 3s states at plasma densities corresponding to the KrF critical surface.

In the hot-spot model, the following nonlinearly coupled equations are solved:

$$\frac{dN_\mu}{dt} = \sum_\nu W_{\mu\nu}(N_e, T_e)N_\nu, \quad \mu = 1, \dots, n, \quad (1)$$

$$N_e = \sum_\mu Z_\mu N_\mu, \quad E_i = \sum_\mu E_\mu N_\mu, \quad (2)$$

$$\frac{d}{dt} \left(\frac{3}{2} N_e k T_e + E_i \right) = S_e - Q_h - R_i - R_{brems} - \frac{3m_e}{m_i} \frac{N_e k}{\tau_e} (T_e - T_i), \quad (3)$$

$$\frac{d}{dt} \left(\frac{3}{2} N_i k T_i \right) = \frac{3m_e}{m_i} \frac{N_e k}{\tau_e} (T_e - T_i), \quad (4)$$

where S_e represents the laser energy absorption rate per unit volume, and Q_h is a phenomenological representation of the heat conduction losses that might occur from the tight focus of a laser-heated plasma. The selenium model contains $n=189$ states and population densities, $\{N_\mu\}$. $\{Z_\mu\}$ and $\{E_\mu\}$ are the ionic charges and energies of these states. They are coupled by the complete set of collisional ionization and excitation rates and radiative and collisional decay rates, $\{W_{\mu\nu}\}$, described in Ref. (8). The equation of motion, $dE_i/dt = Q_i - R_i$, is derived from Eqs. (1). R_i is the sum of optically thin line and free-bound radiation loss rates, which are obtained from the radiation terms in the rate equations (Eqs. (1)). Q_i is the rate of inelastic collisional energy transfer from the electrons to the ions, which is balanced in collisional-radiative equilibrium (CRE) by R_i . R_{brems} is the rate of bremsstrahlung losses from the plasma. In picosecond-heated plasmas, both R_i and R_{brems} are negligible relative to S_e , Q_h , and the rate of thermal energy transfer from the electrons to the ions, given by the last term on the right hand side of Eq. (4), which is proportional to $T_e - T_i$. The expression for this term is taken from Braginskii.¹² It is inversely proportional to the electron-ion collision time τ_e .

The expression for Q_h , taken from Ref. (10), like S_e , is proportional to τ_e . Q_h is also determined in terms of a free parameter, the electron temperature gradient scale length, ℓ_e . This scale length allows one to phenomenologically estimate the maximum effect of heat flow energy

losses on the time history of the electron temperature, T_e . These losses are averaged over the volume of an absorption sphere, i.e., a sphere whose radius, r , is roughly of the order of the inverse bremsstrahlung absorption length of the laser radiation near the critical surface. Thus, the expression for Q_h used in these calculations is:

$$Q_h = \frac{3\kappa_e T_e}{r\ell_e} \cong 12.0 \frac{N_e k T_e}{m_e} \tau_e \frac{3T_e}{r\ell_e}. \quad (5)$$

whenever Q_h is less than a free streaming limit, $Q_h^{fs} = 0.3 N_e k T_e v_{thm}$, where $v_{thm} \equiv \sqrt{2kT_e/m_e}$. Otherwise, Q_h is set equal to Q_h^{fs} .

We consider the physical situation in which a prepulse is used to generate a blowoff plasma containing ion densities that will produce a critical surface corresponding to the 0.25 μm wavelength of a KrF laser when fully ionized. The electron density of a 0.25 μm wavelength laser is $N_e^c = 1.8 \times 10^{22}$. The main KrF pulse can then be used to resonantly heat and ionize selenium near this surface where the ion density is $\leq 7 \times 10^{20}$. At this density, the gains of the J=0-1 and J=2-1 lines at 1 keV would be either zero or near zero, if the plasma were in (CRE).⁸ We assume that the blowoff plasma has a sufficiently small scale length that a substantial portion of the main laser pulse will then be absorbed at or near the critical surface by resonant inverse bremsstrahlung.¹³ Near the critical surface, laser absorption occurs at a rate given by $S_e(t) = \kappa_L(t)I_L(t)$, where I_L is the incident laser intensity and κ_L is the absorption coefficient given, from Refs. (10) and (13), by

$$\frac{1}{\kappa_L} = \frac{8.3 \times 10^9 T_e^{3/2} (1 - N_e/N_e^c)^{1/2}}{(N_e^2/N_i) \ln \Lambda (N_e/N_e^c)}. \quad (6)$$

$\ln \Lambda$ is the Coulomb logarithm and N_e^c is the critical electron density corresponding to 0.25 μm radiation.

Eqs. (1)-(6) describe the resonant inverse Bremsstrahlung heating of a small volume element of plasma whose electrons are cooled by both electron-ion elastic and inelastic collisions and, phenomenologically, by (potentially large) flux limited, heat conduction energy losses. The volume element used in our calculations has a fixed ion density of 6×10^{20} and a fixed radius of 10 μm , which is of the order of the laser absorption length. This volume element is heated with a KrF laser pulse of 2 picoseconds FWHM. Figs. (1) and (2) show a typical response of the temperature and ionization, respectively, to a Gaussian laser pulse of peak intensity, $I_L^{max} = 2 \times 10^{15} \text{ W/cm}^2$.

In order to illustrate the rapidity of the ionization, we began these calculations with a cold (~ 2 eV) weakly ionized plasma. The laser pulse peaks at 3 picoseconds, and the scale length for heat conduction losses was initially taken to be 6 \AA so that heat losses were flux limited for roughly the first two picoseconds of the calculation.

Because large heat losses are simulated in this calculation, the electron temperature, which had a peak above 1400 eV at 4 ps, fell quickly to 700 eV at 10 ps. The rise in the ion temperature as well as the rapid ionization, which reached the neon-like ionization stage in 6 ps (Fig. (2)), also contributed to the cooling of the electrons, but to a lesser degree. However, in spite of this cooling, the plasma continued to ionize over the entire 10 ps interval because the rise in ionization lagged the rise in T_e and because T_e reached such a large peak. Note that, at 6×10^{20} ions/cm³, selenium ionizes rapidly to the neon-like ionization stage before the ionization is slowed by the much larger excitation energies of the L-shell compared to the M-shell. At 6×10^{20} ions/cm³, therefore, selenium is an ideal candidate material for generating population inversions within the Ne-like ionization stage on the 10 picosecond time scale of this calculation.

Because the ion temperature is low, Doppler broadening is only a small correction to collisional broadening of the lasing lines in these calculations. Therefore, Voigt profiles were needed to compute the gains of the J=0-1 lines at line center.¹⁴ $g = (A\lambda^2/8\pi)(N_u - (g_u/g_l)N_l)/\Delta\nu_V$, where A is the radiative decay rate for the transition, λ is the radiated wavelength, and $\{N_u, g_u\}, \{N_l, g_l\}$ are the populations and degeneracy factors of the upper and lower states of the transition respectively. For the value of a Voigt profile at line center, $1/\Delta\nu_V$, we used an expression derived by J. Apruzese:¹⁵

$$\frac{1}{\Delta\nu_V} \cong \frac{1+a}{1+1.66a+1.772a^2} \frac{1}{\sqrt{\pi}\Delta\nu_D}, \quad (7)$$

where $\nu_D = \sqrt{2kT_i/(m_i c^2)}(c/\lambda)$ is the Doppler linewidth and $a \equiv \Gamma_T/(4\pi\Delta\nu_D)$ is the Voigt parameter. Γ_T is the sum of the inverse lifetimes (radiative plus collisional) of the upper and lower states. In our atomic model, these linewidths are approximately 100 m\AA for both J=0-1 lines. Moreover, the calculated J=2-1 linewidths were roughly 1.5 times larger than those of the J=0-1 lines. These results benchmark reasonably well against recent experiments,⁶ in which a 50 m\AA linewidth was measured for the J=2-1 line at 206 \AA . Furthermore, it was speculated that collisional effects were playing a significant role in determining the line profile.

In the calculation under discussion (see Figs. (1) and (2)), the gains of the J=0-1 lines had roughly the time behavior of T_e ; namely, they acquired nonzero values after 4 ps, and they peaked at 5.5 ps. Then, they steadily fell to roughly 1/3-rd of their peak values at 10 ps. As the laser intensity, I_L^{mas} , of the 2 ps pulses was varied, the size of the J=0-1 population inversions varied, depending directly on the amount of laser energy deposited in the plasma. This behavior is shown in Fig. (3). For $I_L^{mas} = 2 \times 10^{15}$, corresponding to Figs. (1) and (2), the maximum gain, g_{mas} , of the 182 Å J=0-1 line was 224 cm^{-1} , while the J=0-1 line at 169 Å achieved a maximum gain of 87 cm^{-1} . However, g_{mas} continued to rise as I_L^{mas} was increased. Beyond an intensity of $3 \times 10^{16} \text{ W/cm}^2$, the 182 Å line is predicted to reach gains in excess of 600 cm^{-1} . The FWHM of the ASE pulses that would be generated in these plasmas is predicted to be 2 ps. The propagation distance of a 2 ps x-ray pulse within an amplifying medium is 0.6 mm.

One problem associated with the gain models that have been constructed to date to describe the population dynamics of the selenium neon-like ionization stage is that they predict the largest gain for the J=0-1 line at 182 Å. In long pulse x-ray laser experiments, however, larger gains were measured for the J=2-1 lines. This problem was discussed in Ref. (8), where it was noted that a factor of two decrease in the magnitude of the calculated monopole excitation cross section, which couples the neon-like ground state to the (upper) 3p state of this 182 Å transition, was sufficient to reverse the relative magnitudes of the J=0-1 and J=2-1 gains in CRE at an ion density of 10^{19} . The effect that such a cross section reduction has in these short-pulse calculations is shown by the dashed curve in Fig. (3). This reduction in the monopole rate produced less than a factor of 2 reduction in the peak gain of the 182 Å line because this line is strongly pumped from the uppermost of the J=1, 3d states. Moreover, this rate reduction did not significantly change the gain of the 169 Å line.

Three factors combine to produce the large gains seen in Fig. (3). One, the calculations are carried out at an ion density that is larger than, by over an order of magnitude, the densities of the gain medium inferred in the long-pulse x-ray laser experiments. Thus, collisional excitation rates are also an order of magnitude larger. Two, the plasma ionizes through a succession of highly non-equilibrium states. Hence, by the time neon-like ground states are plentiful, the electrons are already hot enough to ionize the plasma into the higher ionization stages of the L-shell, well beyond the neon-like stage. Under these conditions, unlike those found in CRE plasmas, there is no

exponential temperature dependence to the ground state excitation rates, and, consequently, they are larger than they would be in CRE. Finally, the populations of the 3d states that feed the $J=0$, 3p states are suppressed in CRE relative the other metastable 3d states due to strong radiative decays to the ground state. The opposite is true during transient excitation, i.e., strong radiative decays imply that the collisional excitation rates of these 3d states are also strong. (In our calculations, they are roughly one to two orders of magnitude larger than the excitation rates to the other ten, metastable 3d states.) Thus, the two 3d states that strongly couple collisionally to the 3p $J=0$ states are relatively overpopulated, rather than underpopulated, and their role in populating the 3p states is significantly enhanced compared to CRE calculations.

Figs. (1)-(3) define the intensity and pulsewidth requirements for a short-pulse laser that would be needed to carry out the above x-ray laser experiments. Fig. (4) roughly defines the energy requirements of the laser. It shows the amount of energy per unit mass that was absorbed in each of the above calculations. For example, a cylinder $10\ \mu\text{m}$ in radius and $0.5\ \text{mm}$ in length containing 6×10^{20} ions/cm³ contains 1.25×10^{-2} μg of selenium. According to Fig. (4), heating this cylinder with a 2 ps laser pulse at 3×10^{16} W/cm² would require 5.4 J of energy. In addition to this energy, one must factor in the laser energy absorbed in other portions of the blowoff plasma as well as reflected energy.

At the laser intensities used in these calculations, highly non-Maxwellian electron distributions will be generated by intensity of the inverse Bremsstrahlung heating.^{16,17,18} At any given level of ionization, these distributions will enhance the rates for exciting the plasma, and, thus, they will lead to larger population inversions than were attained for the calculated gains shown in Fig. (3). Hence, there is reason to believe that the calculated gains shown in Fig. (3) are smaller than may be achieved in an actual short-pulse KrF experiment. Another effect of the non-Maxwellians will be to alter the values of κ_L , κ_e , and τ_e that are needed in the hot-spot calculations. For example, Langdon¹⁶ calculated a factor of two reduction in κ_L due to these non-Maxwellian distributions. Thus, they will cause both upwards and sideways shifts in the Fig. (3) gain curves.

The effects of generating an ion-acoustic turbulence at the critical surface can also significantly affect the gain curves of Fig. (3). Some of the more important effects of this microturbulence might be modeled through the introduction of a single parameter, β ,¹⁸ which modifies a number of important plasma properties. For example, laser absorption would be increased: $\kappa_L^{ia} = \kappa_L(1 + \beta)$,

and the electron-ion collision time, $\tau_e^{eff} \equiv \tau_e/(1 + \beta)$, would be reduced leading to inhibited electron heat flow, $Q_h^{eff} \equiv Q_h/(1 + \beta)$, and increased coupling between the electron and ion thermal energies (see Eq. (4)). Higher ion temperatures would increase the amount of Doppler broadening and somewhat lower the gains that would be calculated at line center under fairly mild levels of saturated ion-acoustic turbulence. Moreover, as shown in Ref. (18), β could acquire values between 1 and 5 at the plasma densities used in these calculations if a saturated microturbulence could be generated. However, determining the levels of microturbulence that can actually be generated in short-pulse experiments is a problem currently under investigation.¹⁹

Because x-ray laser performance is a sensitive measure of underlying plasma conditions, the observation of x-ray lasing in short-pulse experiments would provide important tests of the theoretical models that are used to describe laser absorption, transient ionization, and x-ray laser pumping. The peak of the electron temperature increases in much the same way as the absorbed laser energy as a function of I_L^{mas} (Fig. (4)). The simultaneous measurement of this temperature along with the J=0-1 gains would provide useful experimental information on the presence and influence of microturbulence and non-Maxwellian electron distributions on underlying critical surface absorption phenomena.

Acknowledgement

This work was sponsored by the Ballistic Missile Defense Office/DFI. The authors would like to thank J. P. Apruzese for his helpful comments and for the benefit of his Voigt profile formula.

References

1. K. Boyer and C. K. Rhodes, "Southwest Conference on Optics", edited by R. S. McDowell, (SPIE, Albuquerque, New Mexico, 1985), 540, pp 196-204.
2. See, for example, "Femtosecond to Nanosecond High-Intensity Lasers and Applications", edited by E. M. Campbell, (SPIE, Bellingham, 1990), 1229.
3. P. Amendt, D. C. Eder, and S. C. Wilks, Phys. Rev. Lett. 66, 2589 (1991).
4. D. L. Matthews et al., Phys. Rev. Lett. 54, 110 (1985).
5. M. D. Rosen et al., Phys. Rev. Lett. 59, 2283 (1987).
6. J. A. Koch et al., Phys. Rev. Lett. 68, 3291 (1992).
7. C. J. Keane et al., J. Phys. B 22, 3343 (1989); R. A. London et al., J. Phys. B 22, 3363 (1989).
8. A. Dasgupta, K. G. Whitney, M. Blaha, and M. Buie, Phys. Rev A 46, 5973 (1992).
9. J. P. Apruzese, Phys. Rev E 47, 2798 (1993). (See also references therein.)

10. K. G. Whitney and J. Davis, *J. Appl. Phys.* **45**, 5294, (1974).
11. K. G. Whitney and M. C. Coulter, *IEEE Trans. on Plasma Sci.* **16**, 552, (1988).
12. S. I. Braginskii, "Reviews of Plasma Physics", edited by M. A. Leontovich (Consultants Bureau, New York, 1965), p. 205.
13. T. W. Johnston and J. M. Dawson, *Phys. Fluids* **16**, 722 (1973).
14. R. C. Elton, "X-ray Lasers", Academic Press, Inc. San Diego, 1990, p. 22.
15. J. P. Apruzese, private communication.
16. A. B. Langdon, *Phys. Rev. Lett* **44**, 575 (1980).
17. P. Alaterre, J. P. Matte, and M. Lamoureux, *Phys. Rev A* **34**, 1578 (1986).
18. K. G. Whitney and P. E. Pulsifer, *Phys. Rev. E* **47**, 1968, (1993).
19. S. C. Wilks, W. L. Kruer, M. Tabak, and A. B. Langdon, *Phys. Rev. Lett* **69**, 1383 (1992).

Figure Captions

Figure 1. Calculated electron (T_e) and ion (T_i) temperatures as a function of time for the case, $I_L^{\text{max}} = 2 \times 10^{15}$.

Figure 2. Calculated average charge state, $\langle Z \rangle \equiv N_e/N_i$, as a function of time for the case, $I_L^{\text{max}} = 2 \times 10^{15}$.

Figure 3. Calculated maximum gains for the two $J=0-1$, $3s-3p$ transitions at 169 and 182 Å versus the maximum KrF laser intensity. The solid $J=0-1$ (182 Å) curve corresponds to no modification of the $J=0$ monopole excitation rate, and the dashed curve corresponds to a factor of two reduction of this rate (see Ref. (8)).

Figure 4. Calculated absorbed energy per micro-gram of selenium as a function of the maximum KrF laser intensity for 2 ps FWHM gaussian pulses.

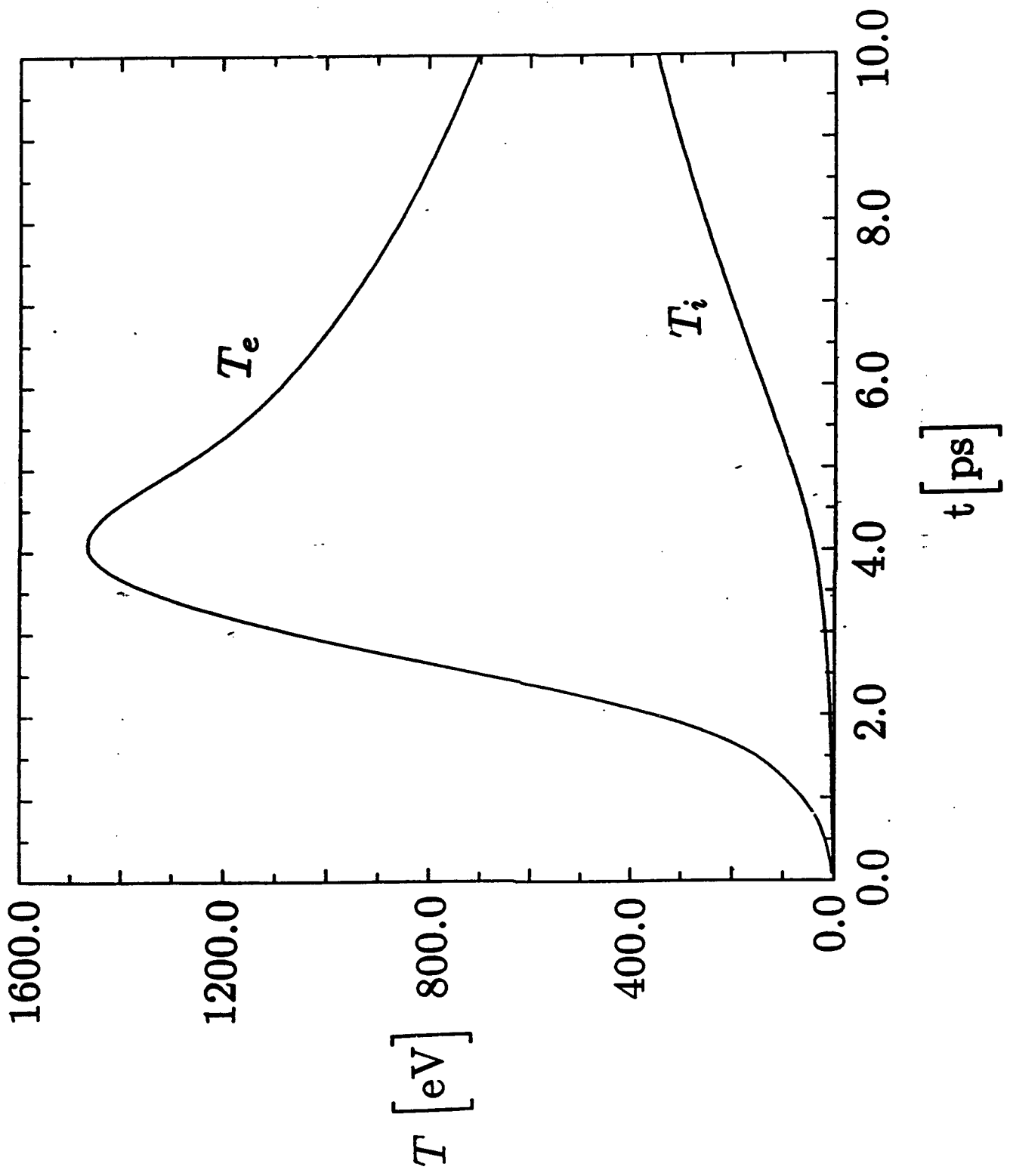


Fig. 1

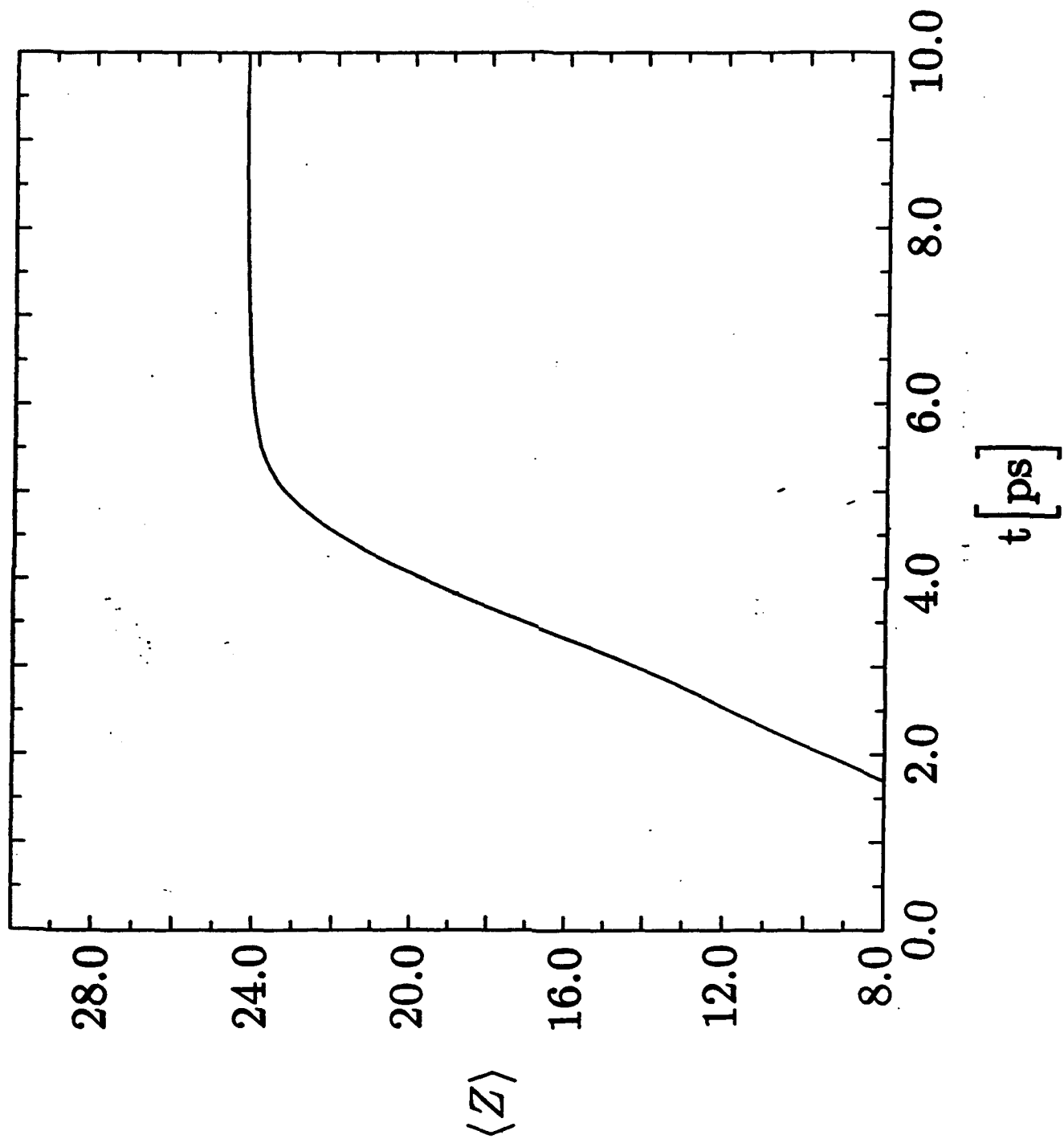


Fig. 2

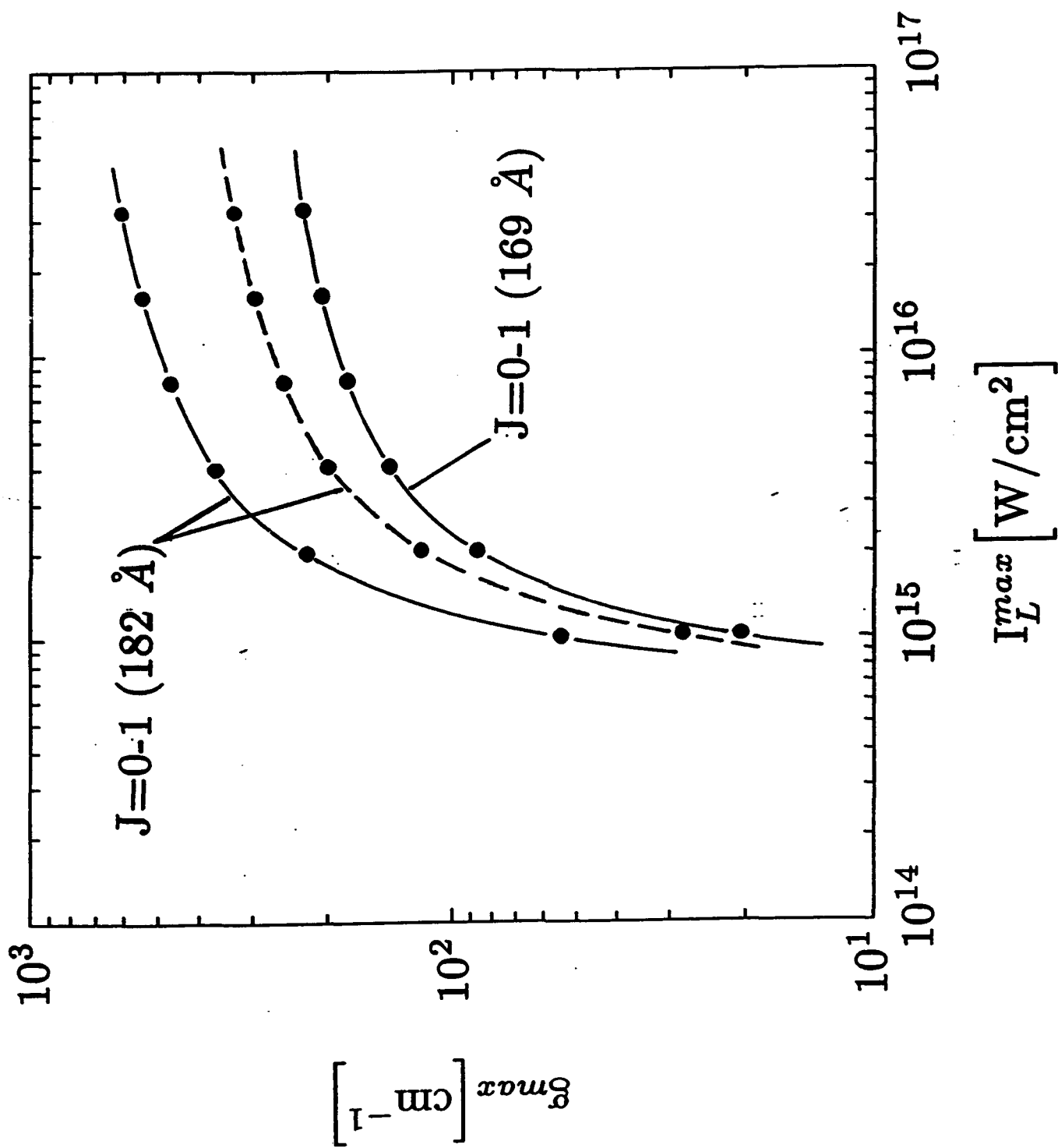


FIG. 3

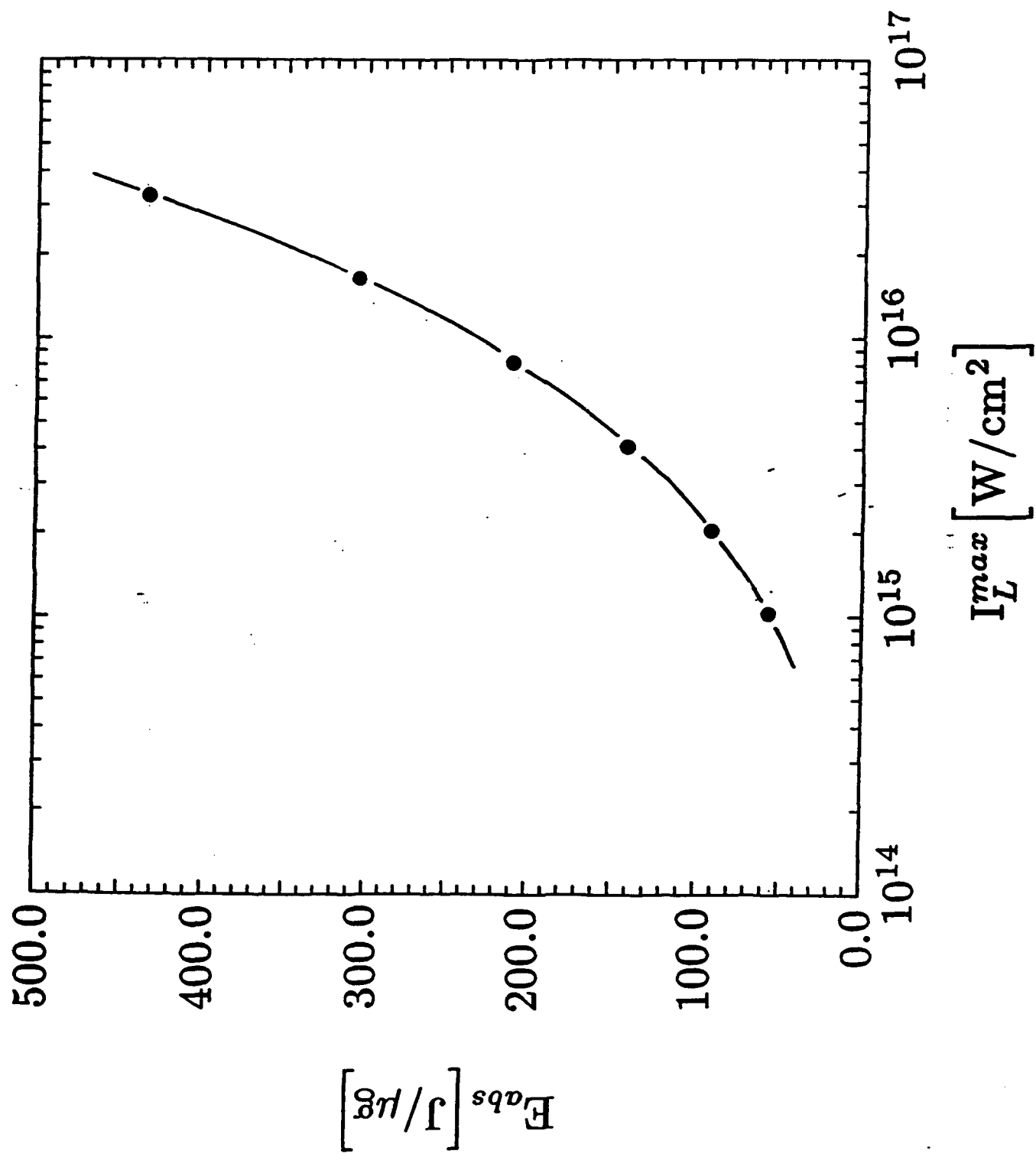


Fig. 4